



UNIVERSITY OF LEEDS

This is a repository copy of *Vertical axis rotation (or lack thereof) of the eastern Mongolian Altay Mountains: implications for far-field transpressional mountain building*.

White Rose Research Online URL for this paper:
<http://eprints.whiterose.ac.uk/129978/>

Version: Accepted Version

Article:

Gregory, LC orcid.org/0000-0001-5525-5447, Mac Niocaill, C, Walker, RT et al. (2 more authors) (2018) Vertical axis rotation (or lack thereof) of the eastern Mongolian Altay Mountains: implications for far-field transpressional mountain building. *Tectonophysics*, 736. pp. 31-46. ISSN 0040-1951

<https://doi.org/10.1016/j.tecto.2018.03.020>

© 2018 Elsevier B.V. This manuscript version is made available under the CC-BY-NC-ND 4.0 license <http://creativecommons.org/licenses/by-nc-nd/4.0/>

Reuse

This article is distributed under the terms of the Creative Commons Attribution-NonCommercial-NoDerivs (CC BY-NC-ND) licence. This licence only allows you to download this work and share it with others as long as you credit the authors, but you can't change the article in any way or use it commercially. More information and the full terms of the licence here: <https://creativecommons.org/licenses/>

Takedown

If you consider content in White Rose Research Online to be in breach of UK law, please notify us by emailing eprints@whiterose.ac.uk including the URL of the record and the reason for the withdrawal request.



eprints@whiterose.ac.uk
<https://eprints.whiterose.ac.uk/>

1 **Vertical axis rotation (or lack thereof) of the eastern Mongolian Altay Mountains:**
2 **implications for far-field transpressional mountain building**

3 Laura C Gregory^{1*}, Conall Mac Niocaill¹, Richard T Walker¹, Gantulga Bayasgalan² and Tim J
4 Craig³

5 *Affiliations*

6 (1) University of Oxford, Department of Earth Sciences, South Parks Road, Oxford OX1 3AN,
7 UK

8 **Present address: University of Leeds, School of Earth and Environment, Leeds LS2 9JT, UK,*
9 *l.c.gregory@leeds.ac.uk*

10 (2) North Carolina State University, Department of Marine, Earth, & Atmospheric Sciences,
11 Raleigh, NC 27695 USA

12 (3) University of Leeds, School of Earth and Environment, Leeds LS2 9JT, UK

13

14 **Abstract**

15 The Altay Mountains of Western Mongolia accommodate 10-20% of the current shortening
16 of the India-Asia collision in a transpressive regime. Kinematic models of the Altay require
17 faults to rotate anticlockwise about a vertical axis in order to accommodate compressional
18 deformation on the major strike slip faults that cross the region. Such rotations should be
19 detectable by palaeomagnetic data. Previous estimates from the one existing palaeomagnetic
20 study from the Altay, on Oligocene and younger sediments from the Chuya Basin in the
21 Siberian Altay, indicate that at least some parts of the Altay have experienced up to $39 \pm 8^\circ$ of
22 anticlockwise rotation. Here, we present new palaeomagnetic results from samples collected
23 in Cretaceous and younger sediments in the Zereg Basin along the Har-Us-Nuur fault in the
24 eastern Altay Mountains, Mongolia. Our new palaeomagnetic results from the Zereg Basin
25 provide reliable declinations, with palaeomagnetic directions from 10 sites that pass a fold
26 test and include magnetic reversals. The declinations are not significantly rotated with respect
27 to the directions expected from Cretaceous and younger virtual geomagnetic poles,
28 suggesting that faults in the eastern Altay have not experienced a large degree of vertical axis
29 rotation and cannot have rotated more than 7° in the past 5 m.y. The lack of rotation along
30 the Har-Us-Nuur fault combined with a large amount of rotation in the northern Altay fits

31 with a kinematic model for transpressional deformation in which faults in the Altay have
32 rotated to an orientation that favours the development of flower structures and building of
33 mountainous topography, while at the same time the range widens at the edges as strain is
34 transferred to better oriented structures. Thus the Har-Us-Nuur fault is a relatively young fault
35 in the Altay, and has not yet accommodated significant rotation.

36 **Key Words**

37 **Vertical axis rotation, strike slip faults, active faulting, palaeomagnetism, central Asian**
38 **tectonics**

39 **1. Introduction**

40 Where continental crust has structural fabric inherited from previous tectonic regimes,
41 intracontinental mountain building is often accomplished by transpressional or transtensional
42 deformation on structures that are not optimally oriented with respect to the regional stress
43 field (Cowgill et al., 2004; Cunningham, 2005; Scholz et al., 2010; Walker and Jackson, 2004;
44 Weil and Sussman, 2004). This occurs where pre-existing and un-favourably oriented
45 structures are preferentially reactivated instead of developing new, optimally oriented faults.
46 Vertical axis rotations (VAR) combined with strike-slip or oblique faulting plays an important
47 role in accommodating the regional strain field in these intracontinental settings
48 (e.g.Campbell et al., 2013; Cunningham, 2005; England and Molnar, 1990; Walker and
49 Jackson, 2002). Investigating the kinematics of transpressional or transtensional mountain
50 ranges is important for testing different models of continental deformation, such as whether
51 deformation is distributed throughout the lithosphere or localised on major fault zones, and
52 in understanding how large-scale continental strain is accommodated seismically (England
53 and Molnar, 1990; Meade, 2007; Zuza and Yin, 2016). Quantifying the fault kinematics and
54 the crustal rotations in these regions is crucial for reconciling modern-day strain rates derived
55 from geodesy with Quaternary and longer fault slip rates.

56 The India-Eurasia collision provides an excellent natural laboratory for investigating
57 distributed continental deformation. The Asian continent between the Siberian craton and
58 the Indian plate was amalgamated in a series of collisions of microcontinents and fragmented
59 arc complexes over hundreds of millions of years since the late Proterozoic (Badarch et al.,

60 1998; Badarch et al., 2002; Briggs et al., 2009; Cunningham et al., 2003b; Cunningham, 1998;
61 Sengör et al., 1993). This long history has left several geologically complicated zones with
62 strong inherited structural grain, which have been reactivated during the most recent collision
63 with the Indian plate (Figure 1). These zones include the Kunlun, Qilian Shan, Tien Shan, Gobi
64 Altay, Altay, Hanguy, and the Sayan mountain ranges.

65 The Altay Mountains of western Mongolia are located ~2500 km from the India-Asia suture
66 (Figure 1). Despite being at the edge of the actively deforming regions, the Altay region
67 accommodates 10 to 20% of the total shortening from the motion of India based on GPS
68 velocities (Calais et al., 2006; Calais et al., 2003; Gan et al., 2007; Likhnev et al., 2010; Wang
69 et al., 2001; Yang et al., 2008; Zhang et al., 2004; Figures 1, 2). In contrast to the Himalaya and
70 Tien Shan ranges further south, where shortening is predominantly accommodated by thrust
71 faults oriented perpendicular and sub-perpendicular to the convergence direction
72 (Abdrakhmatov et al., 1996; Molnar and Ghose, 2000), much of the deformation in the Altay
73 is accommodated in a transpressive regime through slip on a rotating array of strike-slip faults
74 (Baljinnyam et al., 1993; Bayasgalan et al., 2005; Walker et al., 2006).

75 A tenet of the style of deformation of the Altay is that the region rotates about a vertical axis
76 in order to accommodate NNE—SSW directed shortening along right-lateral strike-slip faults
77 that strike NNW—SSE (Baljinnyam et al., 1993; Bayasgalan et al., 2005). Figure 2b shows a
78 schematic block diagram for rotation in the Altay, though in reality active deformation is
79 distributed across the region on a complicated network of anastomosing faults mapped on
80 Figures 1a and 3. Regional anticlockwise rotation is evident in the comparison between well-
81 defined earthquake slip vectors and the direction of maximum horizontal strain vectors
82 derived from GPS velocities across the mountains: slip vector azimuths are generally oblique
83 to the principal strain axes and parallel to the NNW-striking active faults (Figure 3; Bayasgalan
84 et al., 2005; Kreemer et al., 2014). While vertical axis rotation is a mechanism that can
85 reconcile the geodetic and seismic data, few observations have been made on the longer term
86 geological record of rotation in the region. Evidence of tectonic rotation on a geological time
87 scale, including the amount and time-averaged rates of rotation, can be found by comparing
88 palaeomagnetic declinations in older rocks to the predicted declination of the
89 palaeomagnetic field at the time of deposition of those rocks. There is, however, only one
90 previous study of Cenozoic palaeomagnetic directions in the Altay, conducted by Thomas et

91 al. (2002) on samples collected from the Chuya Basin in the Siberian Altay. Their results from
92 Oligocene to Pleistocene clays and sandstones indicated significant anticlockwise rotations of
93 $39 \pm 8^\circ$ over the past 40 Ma relative to a reference virtual geomagnetic pole (VGP) for Eurasia
94 (Figure 3). Their study found dual-polarity and stable chemical remanent magnetisations,
95 carried by magnetite, which are deviated with respect to the reference pole. They suggested
96 that the measured rotation arises from left-lateral shear along the faults surrounding the
97 Chuya Basin. Recent studies, however, have shown that these faults are, in fact, dextral
98 strike-slip faults, as evidenced by the right-lateral 2003 M_w 7.2 Chuya earthquake (Nissen et
99 al., 2007; Figure 1), indicating that the rotations result from the regional kinematics.

100 In order to contribute to the database of tectonic rotations in the Altay and to investigate the
101 continuity of rotation across the region, we sampled Cretaceous to Pliocene sediments from
102 the Zereg Basin for palaeomagnetic investigation (Figure 3). The Zereg Basin is formed in a
103 transtensional bend in the Har-Us-Nuur fault, and is surrounded by several mountain ranges
104 formed along restraining bends in the fault system (Figures 3 & 4). The relief surrounding the
105 Zereg Basin is relatively young, uplifted only within the last 3–8 Ma on the basis of low-
106 temperature thermochronology studies (Jolivet et al., 2007). There are several motivations
107 for selecting the Zereg Basin as a palaeomagnetic study locality. Appropriate material for
108 palaeomagnetic study is limited in the Altay, and the Zereg Basin is a locality where extensive
109 uplifted Jurassic and younger-aged sediments are preserved (Howard et al., 2003). Good age
110 constraints are also required to interpret palaeomagnetic directions, and in the Zereg Basin
111 stratigraphic ages have previously been determined by several authors (Devyatkin et al.,
112 1975; Howard et al., 2003; Khosbayar, 1973; Shuvalov, 1968, 1969; Sjostrom et al., 2001).
113 Whilst local basin-scale rotations can often overprint the regional rotations that are the focus
114 of this study, the structural evolution of the Zereg Basin is well known based on the excellent
115 exposure of active faults, folds, and uplifted stratigraphic units, and can therefore be
116 corrected for in palaeomagnetic data by restoring sample directions to their tilt-corrected
117 orientations.

118 The degree of Cenozoic rotation along the Har-Us-Nuur fault in the Zereg Basin can also be
119 used to test the age of initiation of faulting and mountain building, given assumptions about
120 how these rates relate to rotation. For example, if the fault bounding the Zereg Basin is
121 relatively young, small amounts of rotation may be expected. Finally we discuss these results

122 in the context of an actively evolving transpressional mountain range and the hazard
123 presented by the strike slip faults.

124 **2. Geological Background**

125 **2.1 Regional setting**

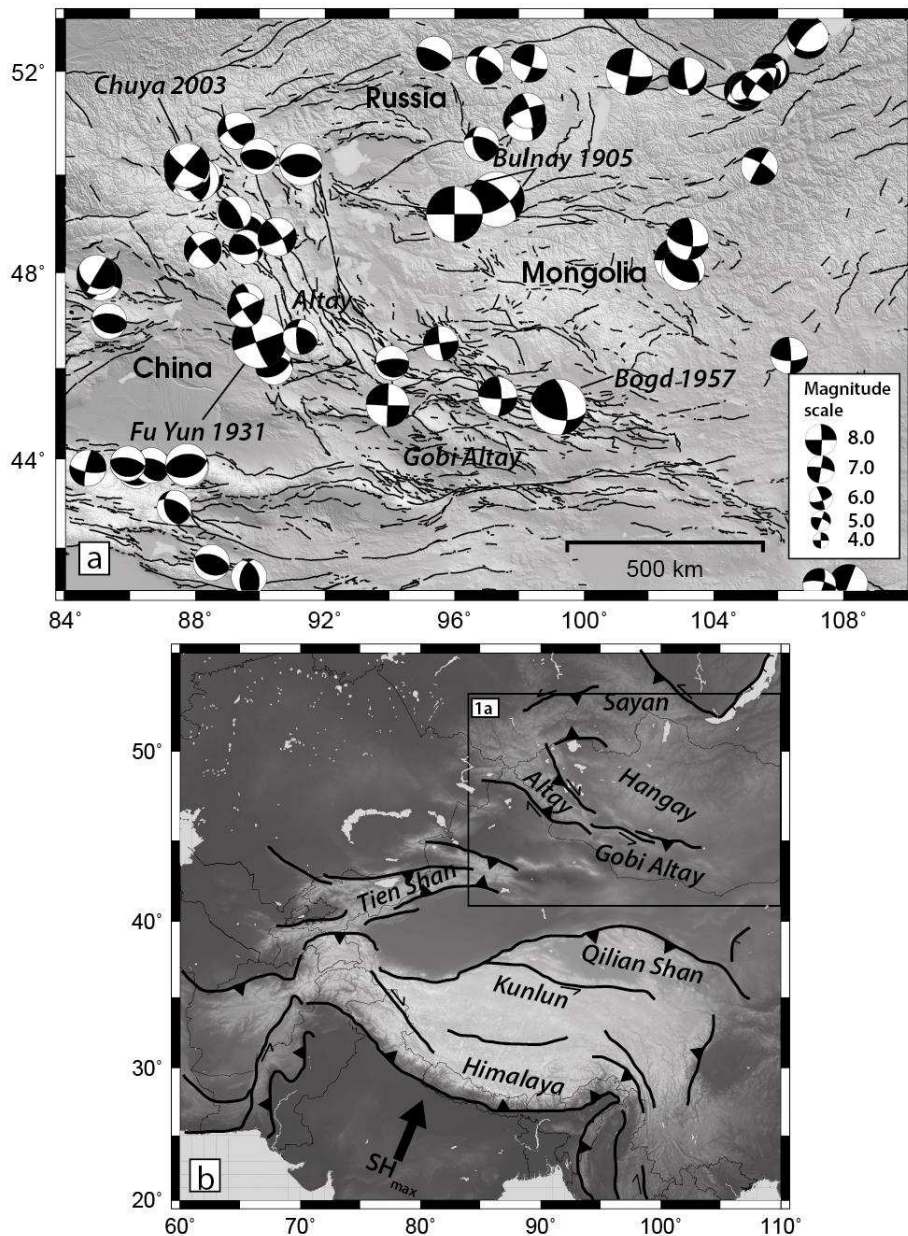
126 Deformation in the Altay is accommodated primarily on a distributed network of long strike-
127 slip faults oriented NNW–SEE, which is oblique to the NNE–SSW oriented maximum
128 shortening direction (Figure 3). Faults follow the dominant structural grain imposed by
129 Palaeozoic deformation during the assembly of central Asia, during which the Altay region
130 was a continental arc setting accreted on the margins of the Siberian craton (Badarch et al.,
131 1998; Badarch et al., 2002; Briggs et al., 2009; Cunningham et al., 2003b; Cunningham, 1998;
132 Sengör et al., 1993). These faults have accumulated several kilometres of right-lateral
133 displacement and are capable of producing up to M_w 8 earthquakes, as shown by historic and
134 prehistoric examples (Baljinnyam et al., 1993; Klinger et al., 2011; Figure 1). A limited number
135 of Quaternary fault slip rates have been determined for the major Altay faults and they range
136 between 0.5–2.5 mm yr⁻¹, with the most rapid rates found on the eastern-most structure: the
137 Har-Us-Nuur fault (Figure 3; Frankel et al., 2010; Gregory et al., 2014; Nissen et al., 2009a;
138 Nissen et al., 2009b). Given the slow time-averaged rate of slip on faults in the Altay, large
139 earthquakes have long recurrence intervals, and any individual fault may have over 1000
140 years between significant events.

141 The cold arid climate of Mongolia allows for good preservation of faulting and deformation
142 features in the landscape, such as pre-historic earthquake ruptures and cumulative
143 Quaternary fault displacements (Baljinnyam et al., 1993; Nissen et al., 2009b; Walker et al.,
144 2006). Also, the high topographic relief of the Altay potentially preserves the total vertical
145 uplift due to Cenozoic deformation, based on the assumption that ancient planation surfaces
146 have been uplifted and preserved without significant erosion on the tops of many mountains
147 (e.g. Jolivet et al., 2007). The highest mountain peaks in the Altay reach over 4000 m, and the
148 region has a high average elevation (~2300 m, Baljinnyam et al., 1993). This is in part due to
149 the elevation of the intervening basins, which are between 1500 and 2500 m in elevation, and
150 thus the overall topographic relief in the range is generally on the order of 2000 m.

151 Conflicting low temperature thermochronology results suggest that the western Altay may
152 have experienced tectonic activity from the early Miocene (~25-20 Ma, Yuan et al., 2006),
153 while workers in the eastern Altay and the Siberian Altay suggest that the full onset of
154 Cenozoic deformation, which has produced the present-day relief in the Altay, did not begin
155 until more recently (having been initiated within the last 8 Myr; De Grave and Van den haute,
156 2002; De Grave et al., 2008; Glorie et al., 2012a; Glorie et al., 2012b; Jolivet et al., 2007;
157 Vassallo, 2006; Vassallo et al., 2007). These authors suggest that the modelled cooling ages
158 from low-temperature chronology is evidence of the onset of the currently active
159 deformation regime due to the preservation of peneplain surfaces on average ~2000 m above
160 the valley floors, which represents the total uplift in the region due to compression from the
161 India-Asia collision. Sedimentation records in the basins surrounding the Altay are consistent
162 with some regional uplift following at least the Oligocene, or ~23 Mya. Sedimentary basins on
163 the eastern margin of the Altay have an Oligocene unconformity, which is overlain by Miocene
164 aged debris-rich fluvial sedimentary units (Cunningham et al., 2003a; Cunningham, 2011;
165 Howard et al., 2003). An increase in conglomeritic deposits in the Plio-Pleistocene in the
166 eastern Altay basins suggest an overall increase in tectonism or that uplift is more proximal
167 to the eastern Altay during the past 5 Myr.

168 The right-lateral faulting in the Altay is in contrast to the faulting directly east of the Altay in
169 the Gobi Altay and along the Bulnay fault zone, where GPS vectors are directed east-west and
170 parallel to the large sinistral faults, requiring no rotation (Figures 1 & 2). The generally NNW–
171 SSE trend of the structural grain in the Mongolian Altay gradually bends to strike E–W in the
172 Gobi-Altay, parallel to the Bulnay fault to the north. The E–W faults are suggested to
173 accommodate the space problem created by rotation in the Altay (Figure 2b; Bayasgalan et
174 al., 2005) as well as a switch to left-lateral shear and eastward motion of central Mongolia
175 with respect to stable Eurasia (Walker et al., 2007).

Figure 1

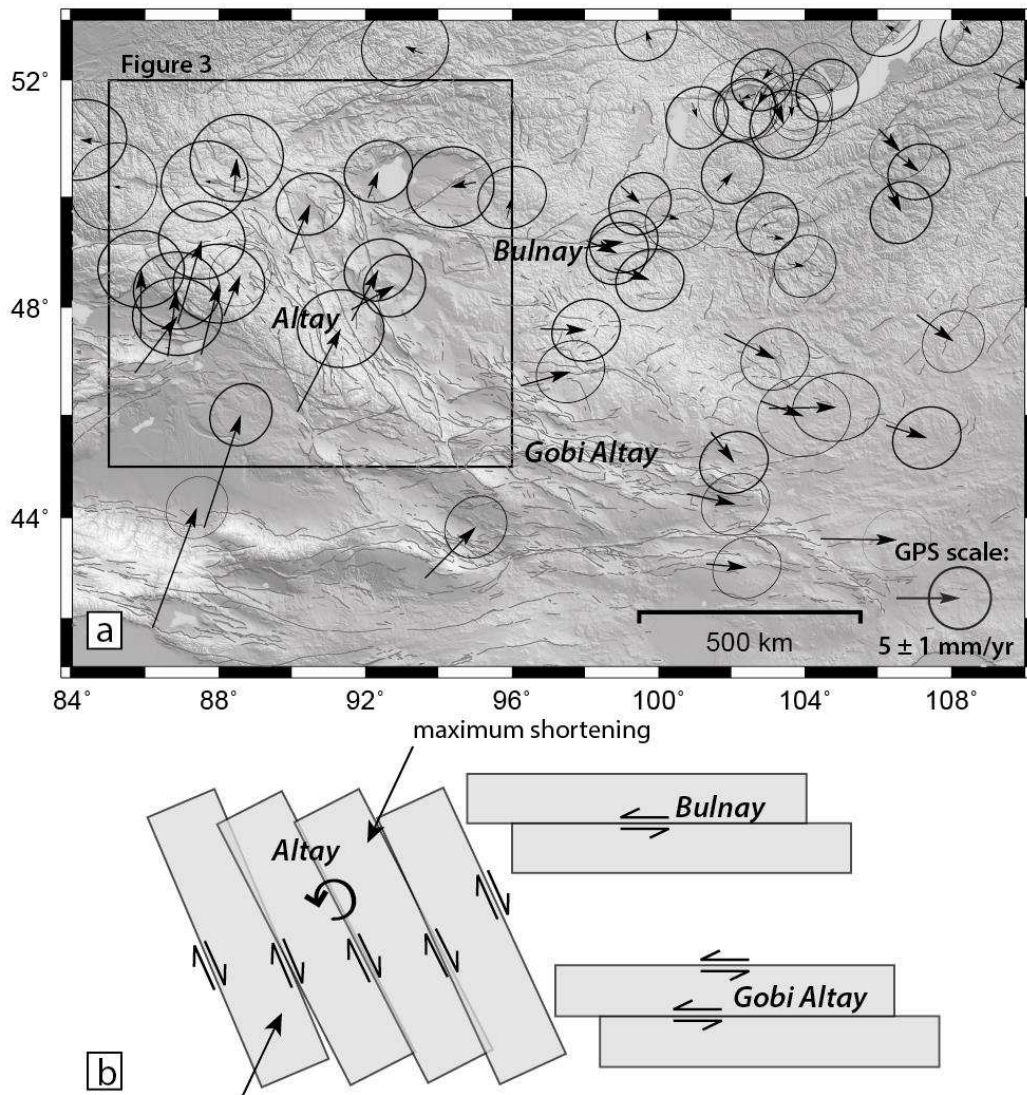


176

177 **Figure 1:** (a) SRTM shaded relief image of the Altay and (b) the India-Asia collision zone,
178 produced using the Generic Mapping Tools software (GMT, Wessel et al., 2013). In (a)
179 earthquake focal mechanisms are from Sloan et al. (2011), Nissen et al. (2007), and
180 Bayasgalan et al. (2005, other references within), with $M_w > 7$ events indicated. Active faults
181 are plotted in black (Baljinyam et al., 1993; Gregory, 2012). (b) SRTM topography and major
182 tectonic boundaries of the India-Eurasia collision.

183

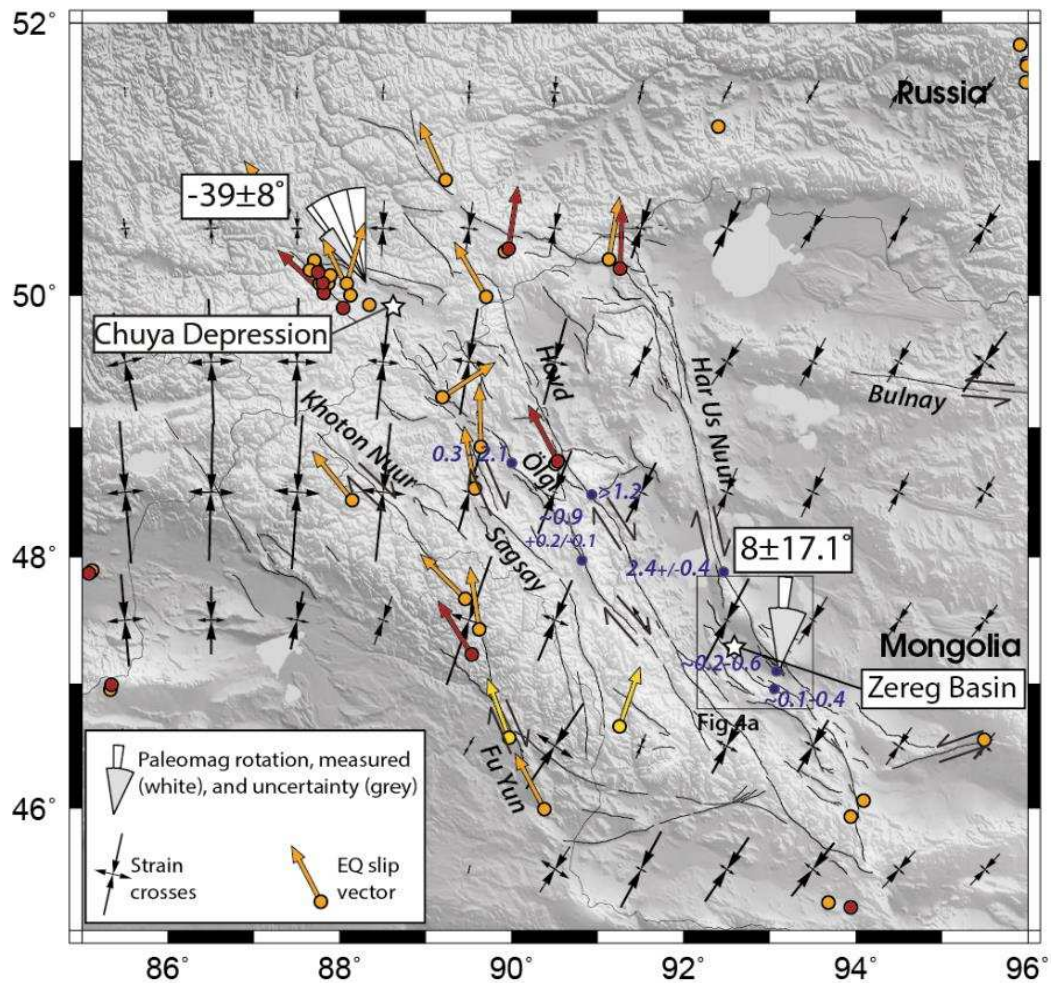
Figure 2



184

185 **Figure 2:** (a) SRTM shaded relief image of the Altay. GPS velocities are relative to stable
 186 Eurasia and suggest ~ 7 mm yr⁻¹ of northeast-directed shortening across the Altay (Calais et
 187 al., 2006; Yang et al., 2008). Active faults are plotted in grey (Baljinnyam et al., 1993; Gregory,
 188 2012). (b) Schematic diagram for deformation in Mongolia, with rotation on dextral faults in
 189 the Altay (W Mongolia), and non-rotational shear required across the Gobi Altay and central
 190 Mongolia, following the pattern of GPS-derived velocity vectors plotted in (a). In this
 191 kinematic model, w indicates the average spacing between faults and θ is the degree of
 192 rotation for an amount d of fault displacement after Walker and Jackson (2004) and described
 193 in section 5.2.

Figure 3



194

195 **Figure 3:** Map of the Altay Mountains and active strike-slip faults. Black strain crosses show
 196 the principal strain axes (compressional arrows point in, extensional arrows point out) from
 197 Kreemer et al. (2014). Quaternary slip rates are noted in blue from Frankel et al. (2010);
 198 Gregory et al. (2014); Nissen et al. (2009a); Nissen et al. (2009b); and Vassallo (2006). Rotation
 199 estimates are plotted as rotational wedges in radians from north (white) with uncertainties
 200 (grey) for the Chuya Basin (Thomas et al., 2002) and Zereg Basin (this study, each wedge
 201 division is 2 radians). Coloured dots (earthquake locations) and arrows (earthquake slip
 202 vectors) are for first-motion mechanisms (yellow; Bayasgalan et al., 2005, and references
 203 therein), waveform-modelled solutions (red; Sloan et al., 2011, and references therein), and
 204 from the Global CMT Catalogue (orange). Earthquake slip vectors are only plotted where the
 205 fault plane is reliably established by field or remote mapping of the active trace. Where
 206 discrimination between the fault and auxiliary plane is not possible, no slip vector is plotted.

207 **2.2 Stratigraphy and structural geology of the Zereg Basin**

208 The Zereg Basin lies between transpressional massifs formed along the Har-Us-Nuur fault,
209 which is the easternmost of the major faults in the Altay (Figure 3). The bedrock exposed in
210 the surrounding mountains comprises Vendian and Palaeozoic metasedimentary and volcanic
211 basement that was intruded by granitic plutons in the Palaeozoic (Devyatkin, 1981; Howard
212 et al., 2003). The Zereg Basin was initially formed as an extensional half-graben during the
213 Jurassic-Cretaceous, and was later reactivated as a transpressional basin in the current
214 tectonic regime (see Figure 15 in Howard et al., 2003). The basin is approximately 140 km long
215 and ranges from 20 to 30 km wide. The Zereg Basin and surrounding mountains are the site
216 of several key studies in the Altay, including Quaternary slip rate studies in Nissen et al.
217 (2009a) and Nissen et al. (2009b), and investigations of the Mesozoic and Cenozoic
218 stratigraphy and structure of the basin and active faults (Cunningham, 2007; Cunningham et
219 al., 1996; Howard et al., 2003; Sjostrom et al., 2001). Continuous outcrops of Mesozoic and
220 Cenozoic strata are exposed in incised drainages along the range fronts of the Jargalant,
221 Bumbat, and Baatar Hyarhan mountains, uplifted by active thrust faults that have propagated
222 into the basin (e.g. Nissen et al., 2009a).

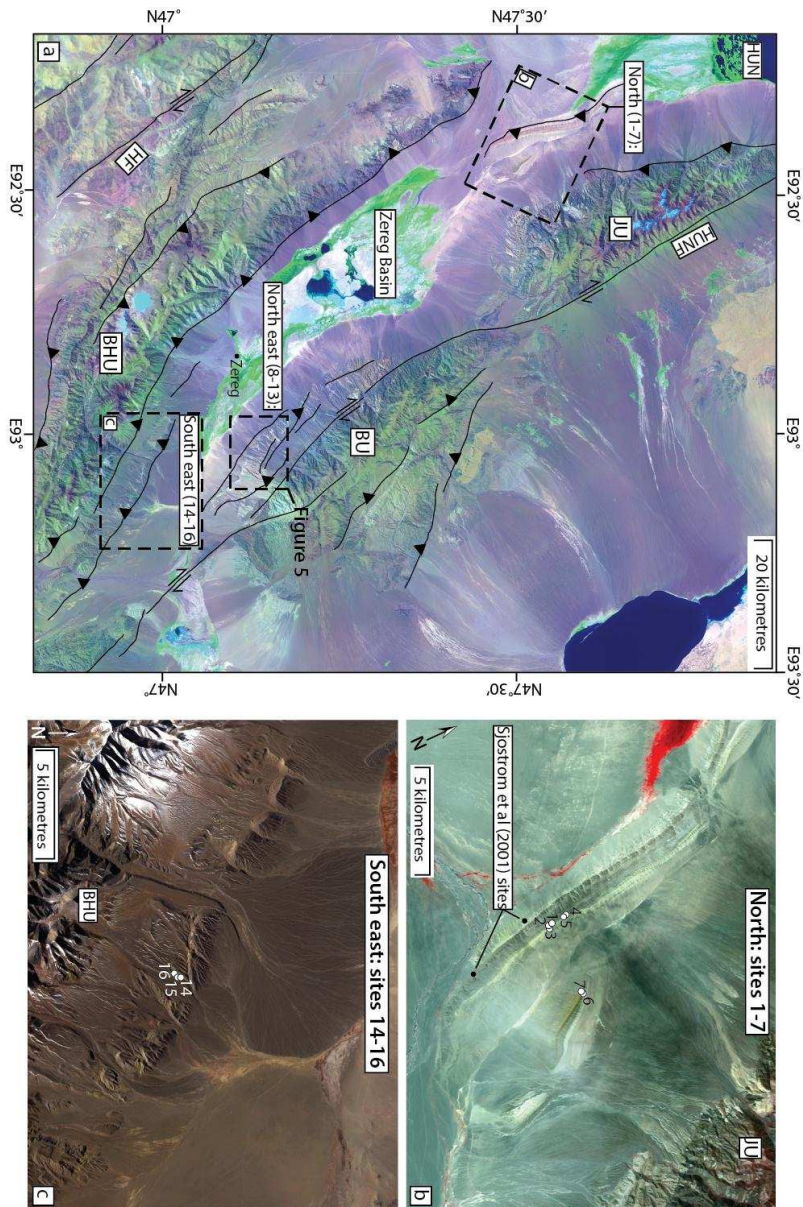
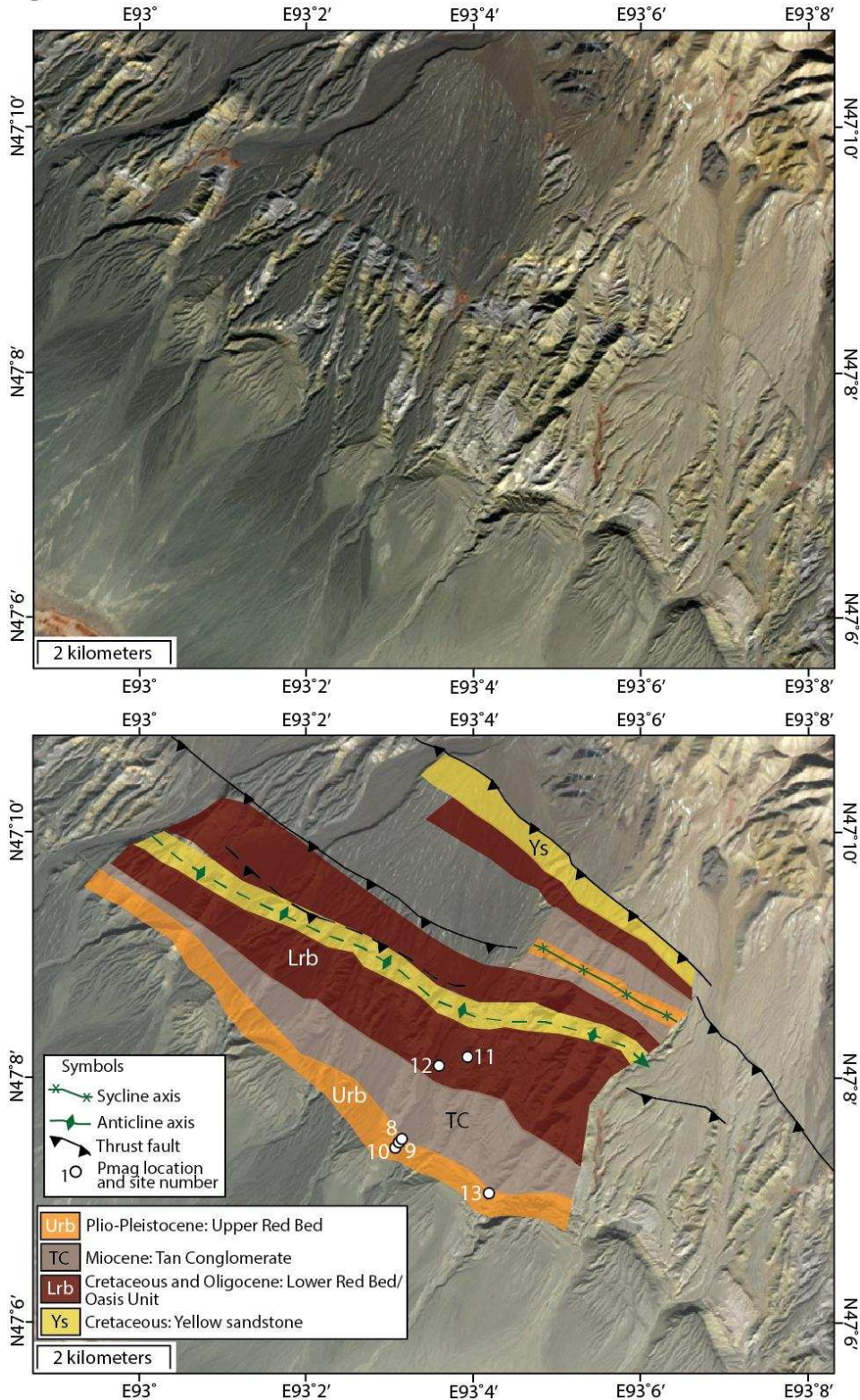


Figure 4

223

224 **Figure 4:** (a) Landsat image (RGB = 741) of the Zereg Basin, with the three different sampling
 225 localities indicated (North, North east, and South west). Figure 4 is indicated by dashed box.
 226 Abbreviations are BHU: Baatar Hyarhan Uul, BU: Bumbat Uul, HF: Hovd Fault, HUN: Har-Us-
 227 Nuur, HUNF: Har-Us-Nuur Fault, and JU: Jargalant Uul. The town of Zereg is indicated. (b) and
 228 (c) are ASTER images of the northern and south-western sampling localities, with sample sites
 229 labelled.

Figure 5



230

231 **Figure 5:** ASTER imagery (15 m/pixel) of the sampling sites from the northeast side of the
 232 Zereg Basin. The lower panel shows a geological map of the area modified from Howard et al.
 233 (2003) and (Nissen et al., 2009a), with the ages of the units mapped labelled and sampling
 234 localities indicated. The region includes a syncline-anticline pair.

235 We briefly summarise the stratigraphy of the sampled sections summarised here based on
236 our observations and previous work. Sjostrom et al. (2001) investigated the sedimentology
237 and provenance of Mesozoic strata and Howard et al. (2003) describe the stratigraphic and
238 structural evolution of the Zereg Basin, both based on extensive field work and previously
239 published palaeontologic work from the Russian literature for the relative dating of
240 sedimentary units (Devyatkin, 1981; Devyatkin et al., 1975; Khosbayar, 1973; Shuvalov, 1968,
241 1969). We targeted units in the Zereg Basin that had been previously investigated in order to
242 have sufficient age control for our palaeomagnetic analyses.

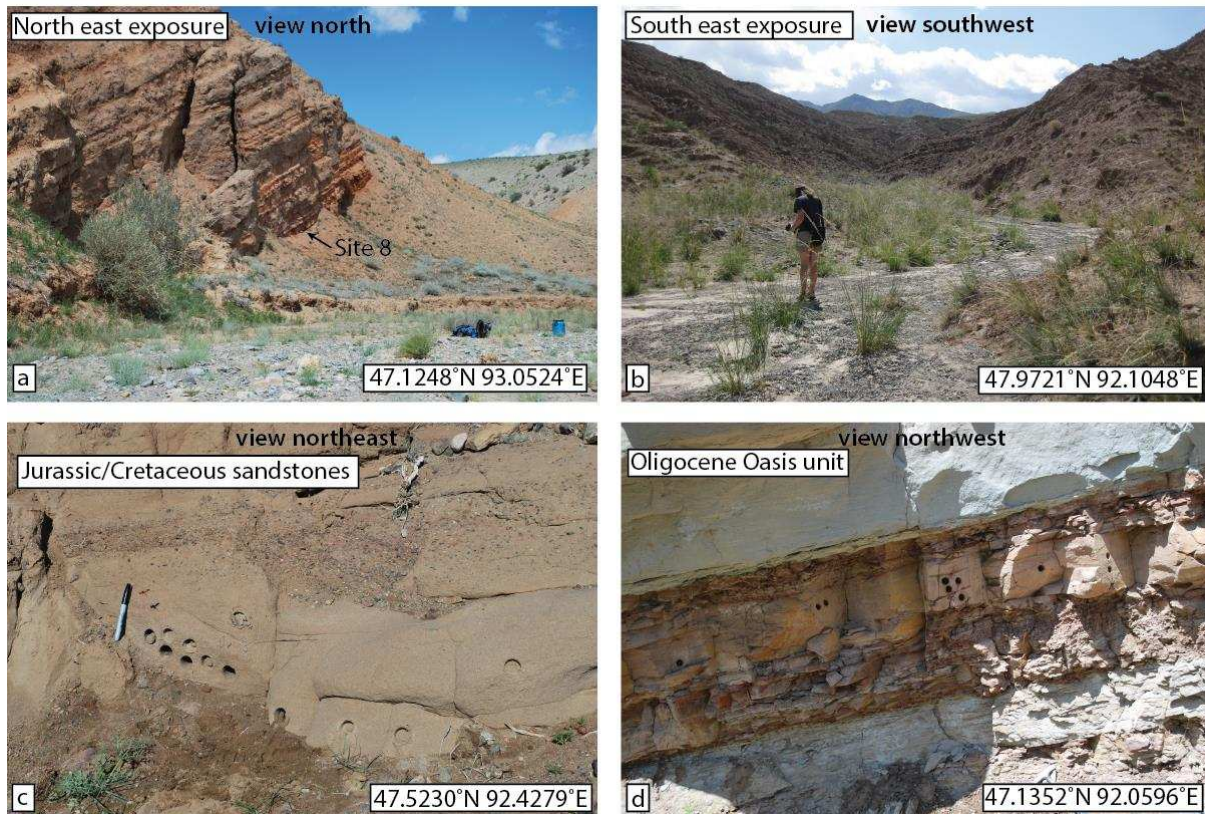
243 The oldest sediments in the Zereg Basin are Jurassic red conglomeritic sandstones, which
244 underlie the sequence and are exposed at the Oshin Nuruu site described by Sjostrom et al.
245 (2001). These are overlain by the oldest named unit in the sequence, the Yellow Sandstone
246 Unit, which is early Cretaceous in age on the basis of fossils belonging to phylum *Mollusca*,
247 class *Ostracoda*, fishes, and a small ornithischian dinosaur (Devyatkin et al., 1975; Howard et
248 al., 2003; Khosbayar, 1973). The Yellow Sandstone Unit is 150 m thick and comprises red
249 pebbly conglomerates below interbedded grey siltstone and buff-coloured sandstone with
250 typically erosive bed bases. Howard et al. (2003) interpreted the unit to represent at the base
251 a lacustrine setting overlain by a succession of sheet floods. They suggest that the top of the
252 unit represents a shallow sand-bed river system deposited in an alluvial setting during a drop
253 in lake level. This unit is exposed on the southwest flanks of Jargalant Mountain, uplifted along
254 two thrust faults developed in the flower structure associated with the restraining bend in
255 the Har-Us-Nuur fault (Figure 4a 'North' box shown in detail in Figure 4b, sampling localities
256 1-7). The Yellow Sandstones are overlain by the up to 450 m thick Lower Red Bed Unit, which
257 is also early Cretaceous (Albian-Aptian) in age on the basis of *Mollusca*, *Ostracoda*, and *Insecta*
258 fossil assemblages (Devyatkin et al., 1975). This unit is characterised by alternating red and
259 grey siltstones with red sandstones. The Lower Red Bed environment is interpreted as
260 periodic inundation of a floodplain or distal alluvial fan setting, deposited from suspension in
261 standing water (Howard et al., 2003). Palaeomagnetic sites 1-7 were sampled from both the
262 buff-coloured sandstones and finer grained layers in the red conglomeritic sandstone in the
263 Jurassic-Cretaceous succession at Oshin Nuruu (Figure 4b).

264 There is an angular unconformity between the Lower Red Beds and the ~140 m thick
265 Oligocene Oasis Unit (Howard et al., 2003). The prevalence of micromammalia establish the

266 Oligocene age of the unit (Devyatkin, 1981). This unit consists of interbedded sandstones and
267 siltstones, with frequent calcium carbonate concretions near the top of the sequence. The
268 unconformity at the base of the Oasis Unit is thought to represent a period of tectonic
269 quiescence and the formation of the early Cenozoic planation surface preserved across the
270 eastern Altay and Gobi Altay. This unit is also thought to originate as part of a distal alluvial
271 fan system that had plenty of accommodation space, based on the lack of evidence for
272 aggradation in channels (Howard et al., 2003). The carbonate concretions may represent
273 extensive caliche development associated with alluvial fan abandonment. We collected sites
274 11-12 from the Oasis unit in fine sandstones and red siltstones, location shown in Figure 5.

275 Miocene-aged sediments are present in the Zereg Basin, but these were too coarse grained
276 for palaeomagnetic analyses and we do not describe them in detail. The overlying sequence
277 comprises the Pliocene –Lower Pleistocene Upper Red Bed, Upper Yellow Conglomerate, and
278 Grey Conglomerate units (Howard et al., 2003). The Pliocene Upper Red Beds are conformable
279 with the Miocene sequence, and mostly comprise interbedded, fining-upwards and red-
280 stained conglomerates and siltstones. This unit is exposed on the northeast and southern
281 sides of the basin, though on the southern side it is referred to as the Upper Yellow
282 Conglomerate Unit by Howard et al. (2003). The Plio-Pleistocene sequence is coarser than
283 underlying sequences, and represents the most recent phase of tectonism in the surrounding
284 mountains. Massive beds with vertical grading indicate the sequence was deposited in a
285 braided stream fluvial or alluvial environment, and evidence of debris flow flooding is
286 occasionally present in clast-supported conglomerate layers (Howard et al., 2003). The Upper
287 Red Beds/Yellow Conglomerate Units are dated as Pliocene based on mammal fossils and
288 fresh water molluscs (Devyatkin, 1981; Howard et al., 2003). Sites 8-10, and 13 on the north
289 east site of the basin and sites 14-16 on the south side of the basin are collected from the
290 most consolidated and fine grained layers within Upper Red Beds (locations indicated on
291 Figures 4a, c, and 5).

Figure 6



292

293 **Figure 6:** Photos of the exposures of Cenozoic and Mesozoic sediments in the northeast and
294 southeast Zereg Basin. (a) Outcrop of the upper red-bed unit, with strata uplifted by
295 southwest-dipping thrust faults (site 8). (b) Upper Red Bed Plio-Pleistocene sediments
296 uplifted on the flanks of Baatar Hyarhan Mountain, dipping SW towards the peaks of Baatar
297 Hyarhan in the background (sites 14-16). (c) Cretaceous sandstones with palaeomagnetic drill
298 holes at site 6. (d) Oligocene Oasis Unit, with interbedded red sandstones (sampled, site 12)
299 and yellow sandstones with cross bedding.

300 **Palaeomagnetic methods**

301 *3.1 Sampling strategy*

302 Oriented palaeomagnetic cores were collected from 16 sites in three different regions of the
303 basin (Figure 4, 6). The three stratigraphic sections sampled are uplifted along different
304 strands of the faults surrounding the Zereg Basin, and as a result, have distinguishable
305 tectonic orientations. Sampling from the same units over a variety of structural orientations
306 adds confidence to the palaeomagnetic results, not only by producing duplicate samples of
307 the same unit in different areas, but also because the sampling strategy helps to determine

308 whether local, fault-related rotations have affected the results. If local rotations have
309 occurred, corrected sample directions from sites of the same age will not necessarily agree
310 across the different sampling localities. The three sampling localities cover the length and
311 width of the basin, and were specifically chosen because each locality has well-constrained
312 Cretaceous and younger stratigraphy.

313 The Jurassic-Cretaceous Oshin Nuruu site on the southwest flanks of Jargalant Mountain was
314 targeted for the northern-most palaeomagnetic sampling site in this study (sites 1—7 in Table
315 1, Figures 4b, 6c). There are two separate exposures uplifted on what were suggested by
316 Cunningham et al. (1996) to be two splay thrust faults related to the main Jargalant faults.
317 The palaeomagnetic sites for analysis were collected from stratigraphically above the Jurassic
318 sections in Jurassic to Cretaceous aged red conglomeratic sandstone units and grey to yellow
319 coarse-grained sandstone units. Sites 1—5 were collected from the sediments uplifted by the
320 western-most thrust fault, and sites 6 and 7 from the units uplifted by the eastern thrust
321 (Figure 4b). Samples were collected from finer grained mudstone and siltstone units
322 interbedded with the conglomerates. Sediments on the eastern ridge are coarser grained,
323 including 1—2 mm sized pebbles within much of the sandstone and mudstone units, and were
324 less consolidated than those from the western ridge.

325 Sites 8 through 13 were collected from Cenozoic strata uplifted in the range front of Bumbat
326 Mountain (Figure 5, 6a). The sites are part of a thrust fault driven syncline-anticline pair that
327 has folded Upper Jurassic to Plio-Pleistocene sediments, which are unconformably overlain
328 by Quaternary alluvial fans. A similar sedimentary sequence is also uplifted on the opposite
329 side of the Zereg Basin, where sites 14—16 were collected (Figure 4a, 4c, 6b). No major folds
330 were identified where we sampled on the southwest side of the Zereg Basin, and the
331 succession consistently dips southwest towards Baatar Hyarhan Mountain.

332 The Cretaceous and younger stratigraphy is divided into four groups: the Cretaceous Lower
333 Red Beds, the Oligocene Oasis Unit, the Miocene Tan Conglomerates, and the Pliocene Upper
334 Red Bed/Pleistocene Conglomerates (Howard et al., 2003; Figure 5b). Two palaeomagnetic
335 sites were collected from the Oasis Unit (sites 11—12), stratigraphically above the
336 unconformable boundary with the Cretaceous Lower Red Beds (Figure 6d). Several sites were
337 sampled from the Pliocene Upper Red Bed Unit on both the north-eastern and south-eastern

338 side of the Zereg Basin. The sediments sampled on the south-eastern side of Zereg (sites 14-
339 16) were similar in colour, sorting, grain size, and stratigraphic relationships between
340 interbedded layers to those sampled on the north-eastern side of the basin (sites 8-10 and
341 13) in the Upper Red Bed Unit, confirming that the same unit is represented on both sides of
342 the basin. All sites were sampled in finer grained and more consolidated layers as these are
343 more reliable for palaeomagnetic analyses. We collected samples from specific localities that
344 had previously determined age constraints as described in section 2.2 and published in
345 Devyatkin (1981); Howard et al. (2003); and Sjostrom et al. (2001).

346 *3.2 Palaeomagnetic sampling techniques and experiments*

347 Samples were collected in the field using a gasoline powered hand drill, and were oriented
348 with a magnetic compass. Due to the low magnetic intensity of the sediments, no correction
349 for magnetic interference from the outcrop was necessary. Over 160 core samples were
350 collected from 16 sites in three different regions of the Zereg Basin (Figure 4, Table 1).
351 Samples were carefully wrapped in the field and further processing was done at the University
352 of Oxford palaeomagnetic laboratory. Core samples were cut into standard sized specimens
353 using a custom saw, and a few delicate samples were cut by hand with a utility knife and then
354 sanded to remove any possible metal contamination from the knife. Samples were stored and
355 measured in a magnetically shielded room, with an internal field <200 nT. A pilot batch of 1-
356 2 specimens from each site was thermally step-wise demagnetised at temperature intervals
357 of 50°C steps up to 500°C, followed by 20°C steps to 620°C, and then by 10°C steps until
358 demagnetised (up to about 700°C). After analysing the preliminary samples, a series of
359 thermal steps up to 700°C were chosen for demagnetisation of the remaining samples
360 (generally at 60°C steps to 540°C, followed by 20°C steps to 700°C). Magnetic measurements
361 were made on samples in between each heating step, on the Oxford 2-G enterprises Model
362 755 3-axis cryogenic magnetometer. Best-fit magnetic components found during
363 demagnetisation were determined for linear segments on orthogonal plots, using the least-
364 square regression analysis implemented in the Super IAPD program
365 (<http://www.geodynamics.no/software.htm>). The orthogonal plot is a display of the
366 horizontal and vertical (declination and inclination) projection of the magnetisation scaled
367 with intensity at each temperature step (Figure 7; Zijdeveld, 1967).

368 3.2 Rock magnetic experiments

369 In order to better characterise the carriers of magnetisation in samples, magnetic tests were
370 performed on samples. Initial susceptibility was measured for all samples, and Curie
371 temperature measurements were carried out on a select group of powdered samples
372 (representing the variety in age and composition in the sampling sites) using a KLY-2
373 susceptibility bridge with a CS2 heating unit (Figure 8). In these experiments, the susceptibility
374 of a finely crushed sample is incrementally measured during heating and cooling. The
375 magnetic carrier can be determined from the change in magnetic susceptibility with
376 temperature, in particular the value for the Curie temperature of the sample, which occurs
377 when the magnetic ordering is destroyed with an accompanying loss of susceptibility (e.g.
378 Merrill et al., 1998).

379 4. Results

380 4.1 Palaeomagnetic data

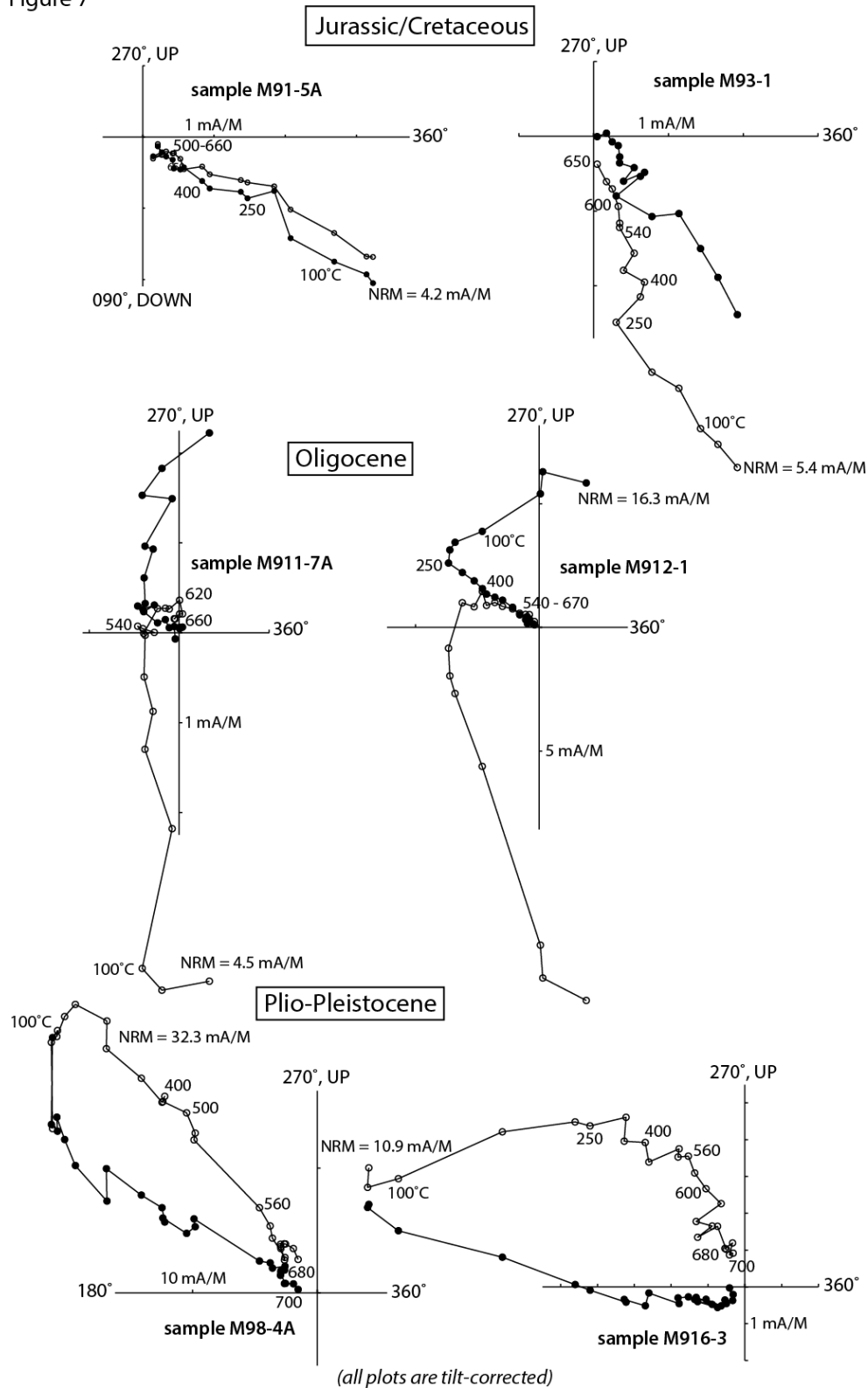
381 Palaeomagnetic data from sites that have consistent and stable remanent magnetisations are
382 listed in Table 2. Representative orthogonal plots and thermal demagnetisation paths are
383 displayed in Figures 6a, b, and c from the three different regions of the Zereg Basin shown in
384 Figure 4. The intensities of natural remanent magnetisations (NRM) range from around 1 to
385 44 mA/m, with generally lower intensities in samples that had less stable directions. Site
386 averaged NRM intensities for sites used in our analyses are listed in Table 2. The highest
387 intensities were found from a site that yielded inconsistent directions and has not been
388 included in the analysis (site 9). A low coercivity component was frequently removed from
389 samples at lower temperatures (up to $\sim 250^{\circ}\text{C}$), which can generally be attributed to the
390 present day field (north and steep, e.g. Figure 7), possibly as a result of recent weathering.
391 Many samples lost a significant percentage of intensity at temperatures up to approximately
392 120°C , which may be indicative of the presence of goethite imparting a chemical remanent
393 magnetisation (CRM, e.g. sample M912-1, Figure 7). However, once this low coercivity
394 component was removed, a stable magnetic direction could generally be found from the
395 higher temperature measurements (e.g. sample M916-3, Figure 7). Samples were fully
396 demagnetised when the intensity of magnetisation is less than 10% of the NRM. Full
397 demagnetisation occurred at high temperatures between $560\text{--}700^{\circ}\text{C}$, indicating that both

398 magnetite and hematite may be contributing to the primary magnetisation in the samples
399 that did not fully demagnetise at 580°C, as the Curie temperatures are 580°C for magnetite
400 and between 675° to 725°C for hematite (Merrill et al., 1998).

401 Both *in-situ* and tilt-corrected directions for the stable high coercivity components are listed
402 in Table 2 and shown in Figure 9. The tilt correction was made for each site based on the strike
403 and dip of the strata sampled (Table 1). In order to test for tectonic rotation of the samples
404 as well as inclination flattening during compaction, the tilt-corrected directions can be
405 compared to the expected VGP (virtual geomagnetic pole) for the time of deposition. VGPs
406 were calculated from the apparent polar wander path (APWP) for Eurasia catalogued by
407 Torsvik et al. (2012) for the Zereg Basin using the GMAP2003 program (available at
408 <http://www.geodynamics.no/software.htm>). The degree of rotation for each site is the
409 difference between the measured tectonic corrected declination (D_{tc}) and the expected
410 declination for a given stratigraphic age based on the VGP. The flattening of a site is the
411 difference between the expected inclination and tilt-corrected, measured inclination (I_{tc}).

412 Uncertainties at the 95% confidence level for the rotation and flattening were determined
413 following methods in Demarest (1983). Uncertainties are based in part on classic Fisher (1953)
414 statistics for the probability distribution of a two dimensional cone of 95% confidence (α_{95}).
415 A small correction factor is added to the uncertainty, in line with Demarest (1983), which
416 takes into account the precision of the results as well as the inclination of samples. The
417 uncertainties for rotation of declinations increase as inclinations steepen, and as inclination
418 approaches 90°, a range of 0—360° for declination is possible.

Figure 7



419

420 **Figure 7:** Example thermal demagnetisation Zijderveld diagrams from each rock unit sampled.

421 Plots are shown tilt-corrected with a tectonic correction for the orientation of the strata

422 sampled. Open points indicate the inclination, and closed points are the sample declination.

423 North is to the right of the plot, and magnetic declinations are fit as vectors through
424 measurements from high to low temperature.

425 Rotations of individual sites from the expected VGP declination are between 22° clockwise to
426 6° anticlockwise. The site rotations are combined into groups based on their stratigraphic age.
427 The majority of samples yield inclinations that are shallower than those predicted from the
428 reference poles by >10°, and have likely experienced inclination flattening. This shallowing
429 phenomenon is common amongst sedimentary rocks due to compaction, particularly in
430 Cenozoic sediments in central Asia, where sedimentary samples are reported to have
431 inclinations that are 20° shallower than expected (Dupont-Nivet et al., 2002; Tauxe and Kent,
432 2004; Thomas et al., 1993). The majority of sites in the Zereg Basin have experienced
433 inclination shallowing of approximately equal to or less than 20°. The exceptions to this are
434 sites 1, 11, and 12, which have experienced significantly more flattening. However, the
435 shallowing of inclinations does not affect the sample declination, and shallowing may also
436 support a primary magnetisation because it is suggested to be acquired during and
437 immediately following sedimentary deposition (Tauxe and Kent, 2004).

438 *4.2 Magnetic tests*

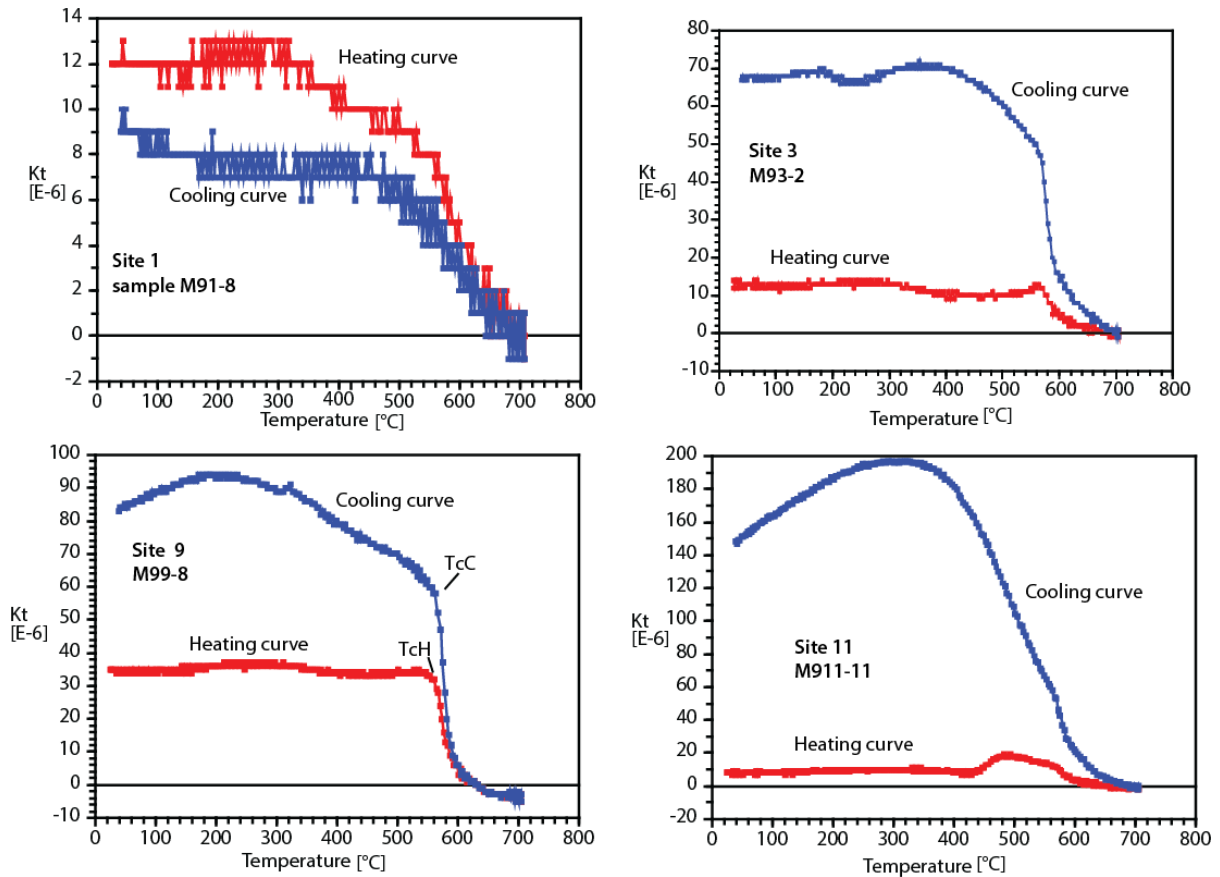
439 The results of susceptibility tests are shown in Figure 8, for select sites that have stable
440 demagnetisation vectors as well as one site with inconsistent directions (site 9). Samples from
441 sites 3, 9, and 11 display a characteristic *Hopkinson* effect, which is an increase in
442 susceptibility just before the Curie temperature drop in susceptibility, and is often associated
443 with the unblocking temperature of the magnetisation (e.g. Tauxe, 2010). The loss of
444 susceptibility around 560°C is characteristic of magnetite being the primary carrier of
445 magnetisation, and most samples display a drop in susceptibility in this range. Some samples
446 also lose the remaining susceptibility around 680–700°C, suggesting that haematite is also
447 present in those samples.

448 In some cases, the statistics of the mean directions from a site are quite poor, with high α_{95}
449 values and low k (kappa) values. Whilst there is no specific acceptable standard for α_{95} and k ,
450 values of $\alpha_{95} < 16$ and $k > 10$ are considered to be typical for good quality studies (e.g. Van der
451 Voo, 1989). Two sites yielded α_{95} values > 16: sites 3 & 6. At site 3 the high α_{95} can be
452 attributed to the low number of specimens, and they yield a perfectly acceptable value of k .

453 At site 6 both the α_{95} value and k lie marginally outside the Van der Voo (1989) criteria, due
 454 to the low magnetic intensity of the specimens. Site 14 yield too few stable directions to
 455 calculate statistics, but the mean direction nonetheless agrees with that from other sites at
 456 that locality.

457

Figure 8



458

459 **Figure 8:** Results from Curie temperature tests on four example samples. TcH indicates the
 460 Curie temperature when heating, which is indicated by a sharp drop in susceptibility. TcC is
 461 the Curie temperature during cooling, and is the end of the steep increase in susceptibility
 462 during cooling. Most samples show some alteration during heating, evidenced by the higher
 463 susceptibility during cooling than heating, although this is not observed in site 1. Samples
 464 have Curie temperatures around 560 – 580°C, indicating that magnetite is the primary
 465 magnetic carrier. Site 3 shows a steepening in slope at around 650°C, which may indicate the
 466 presence of hematite.

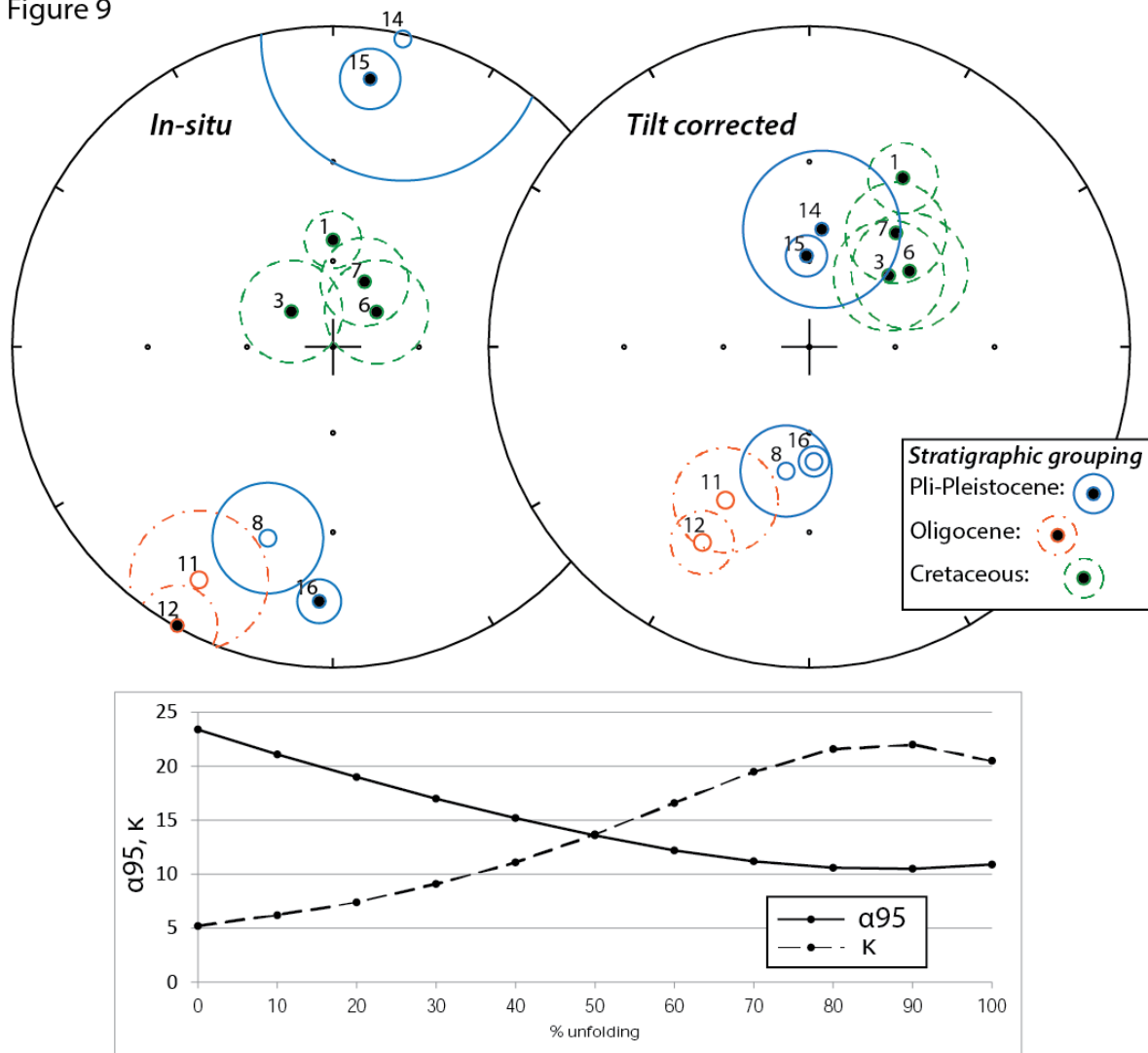
467 **5. Discussion**

468 *5.1 Reliability of data*

469 Each palaeomagnetic site in the Zereg Basin was collected where the stratigraphy had been
470 previously determined and described in the literature (Devyatkin, 1981; Howard et al., 2003;
471 Khosbayar, 1973; Shuvalov, 1968, 1969; Sjostrom et al., 2001). Whilst we cannot place precise
472 age constraint on each locality, we can assign a geological period or epoch on the basis of the
473 previous work and sampling the same sections that other authors have documented. This
474 precision is sufficient for comparison with palaeomagnetic poles in the next section, which
475 are limited to the same level of precision as our lithostratigraphy.

476 Tilt correction of the sites results in better grouping of the mean directions, and directions
477 from all of the sites can be combined into a statistically significant fold test, positive at the
478 95% confidence level, using the classic McElhinny (1964) approach (Figure 9). During the fold
479 test site directions are incrementally restored back to horizontal from the stratigraphic
480 orientations, and α_{95} and K values are calculated for each 10% increment. If magnetic
481 directions in the samples have been reset since deposition and subsequent folding, the
482 scatter of the results (α_{95}) is predicted to worsen and the precision (k: essentially a measure
483 of the grouping of the data) will decrease, due to overprinting of the magnetisation on the
484 structure of the fold. If the directions are primary, the measures of precision and grouping
485 will improve, because the samples migrate to the 'true', tilt-corrected site mean.

Figure 9



486

487 **Figure 9:** *In-situ* and tilt corrected site means and α_{95} cones of uncertainty are shown on the
 488 stereoplots (lower hemisphere projection) for all stable and consistent sites (site numbers
 489 are labelled). Closed circles indicate positive directions and open circles indicate negative
 490 directions, and all sites are plotted as a single (normal) polarity. The lower panel shows the
 491 results of the fold test that includes all sites, with a higher K value, indicating greater
 492 precision, with 90-100% unfolding.

493 Unfolding of the Zereg Basin sites by up to 90% results in a higher k value for the mean of all
 494 sites, which would not be the case if samples were remagnetised during or after tectonic
 495 tilting occurred. This positive fold test confirms that the isolated magnetic components are
 496 primary. Fold tests were also performed on groupings of the sites by age, but none of the
 497 groups produced a statistically significant fold test. This is likely because there is little

498 variability in bedding orientations within each age group, and the fold tests would be
499 improved by sampling from units of the same age, but from strata with variable orientations.

500 Also attesting to primary magnetisation are several sites that have reversed polarity,
501 exhibited in the Cenozoic sequences (Figure 9). While this is not necessarily confirmation of
502 primary magnetisation, it does add confidence to the reliability of the directions because if
503 overprinted, generally all samples will have the same polarity. Tilt-corrected directions are
504 distinct from the present day field in the region, which has a north declination and a steep
505 inclination of approximately 65° , suggesting that the measured directions are not the result
506 of a present-day overprint. A steeply dipping, northerly overprint was found at low
507 temperatures in several sites, but this component was removed by stepwise heading (e.g.
508 sample M912-1, Figure 7, Oligocene group). Finally, the presence of significant shallowing of
509 the inclinations is also supportive of a primary origin for the magnetization, because such
510 shallowing occurs shortly after deposition during compaction and consolidation of the
511 sediments.

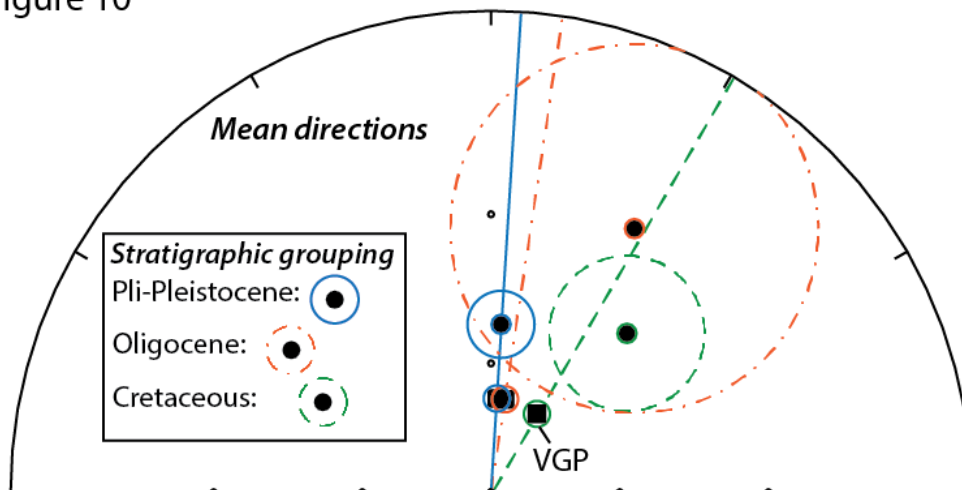
512 *5.2 Lack of rotation of the Zereg Basin*

513 The mean palaeomagnetic directions measured from each of the Jurassic-Cretaceous,
514 Oligocene, and Plio-Pleistocene sediments are displayed in Figure 10. The predicted
515 declination and inclination for the samples, based on VGPs for stable Eurasia transformed to
516 the Zereg basin locality, calculated from Torsvik et al. (2012), are also shown as squares on
517 the same figure with dashed lines indicating the predicted declination. The mean inclinations
518 are shallower than what is expected from the VGPs, confirming that some degree of flattening
519 has occurred, probably as a result of compaction. The mean declinations are similar to those
520 predicted by the VGPs, and even the oldest group is well within the 95% cone of uncertainty
521 of the expected declination (Jurassic/Cretaceous $D=40.6^\circ \pm 15.4^\circ$, compared to the VGP
522 $D=30.4^\circ \pm 3.0^\circ$). The Plio-Pleistocene grouping has the lowest uncertainty, and the mean
523 declination is not rotated with respect to the expected declination (Pliocene $D=003.4^\circ \pm 7.1^\circ$,
524 compared to a VGP $D=003.5^\circ \pm 3^\circ$).

525 The results from the Zereg Basin suggest that the region has not undergone a measurable
526 amount of palaeomagnetic rotation since the deposition of the Jurassic/Cretaceous
527 sediments. The results are of high quality, and pass several field tests that attest to primary

528 magnetisation, including reversal and fold tests. The ages of the strata are generally well
 529 defined, based on paleontological work, geologic mapping, and stratigraphy (Devyatkin et al.,
 530 1975; Howard et al., 2003; Sjostrom et al., 2001). The lack of rotation in the Zereg Basin is in
 531 strong contrast with both the existing palaeomagnetic results from the Chuya Basin in the
 532 Siberian Altay (Thomas et al., 2002), and with the anticlockwise rotations predicted by
 533 geodetic data and the pattern of faulting in the Altay (Bayasgalan et al., 2005; Cunningham,
 534 2005). In the Chuya Basin, anticlockwise rotations of $39^\circ \pm 8^\circ$ have been suggested on the
 535 basis of palaeomagnetic data from Oligocene and younger aged sediments, with reasonable
 536 tests of reliability. Even if a proportion of the rotation in the Chuya Basin is due to local basin-
 537 scale rotations, the contrast between palaeomagnetic results from the two localities in the
 538 Altay is significant.

Figure 10



539
 540 **Figure 10:** Age mean palaeomagnetic directions compared to the reference VGP poles we
 541 calculated for Mongolia (Torsvik et al., 2012). Our directions reflect some inclination
 542 shallowing but no rotation of the declination, within the error of the measurements.

543 Using the kinematic relationship in Walker and Jackson (2004), we can calculate a rotation
 544 rate for the Altay of 1.9° to 3.8° per million years, assuming that the faults slip on average 1-
 545 2 mm yr^{-1} and are spaced on average 30 km apart (w and d in figure 2, respectively). We also
 546 calculate the rotation rate in the Chuya Basin using the total rotation reported and the age
 547 (mid-Miocene and younger) of the sampled sediments. This is a minimum rate calculated with
 548 the assumption that rotation was ongoing as the sediments were deposited (e.g. if rotation
 549 initiated sometime after deposition, this would require the rotation rate to be faster).

550 Assuming a rotation of 39° and sediment age of 14 Ma, the rotation rate in Chuya would have
551 to be nearly 3° per million years, which agrees with the kinematic rotation rate of 1.9° to 3.8°
552 calculated on the basis of the rate of fault slip and fault spacing. For comparison, we estimate
553 a maximum rate of rotation for the Zereg basin permissible by the resolution of our
554 palaeomagnetic data. The best-resolved mean direction comes from the Plio-Pliocene age
555 group, which has a 95% confidence window of 7° ($D=003.4^\circ \pm 7.1^\circ$, Figure 10). Therefore, the
556 Zereg basin must have rotated less than 7° since ~5 Ma, and the averaged rotation rate must
557 not exceed 1.4° degrees per Ma over that period. This can be accommodated either by having
558 a very young fault (less than 2.5 Ma) and rates comparable to those measured elsewhere in
559 the Altay (3° per million year as in the Chuya Basin), a significantly slower rate of rotation over
560 the time the fault is active, or some combination of these two scenarios.

561 Nissen et al. (2009b) estimate that the initiation age of the Har-Us-Nuur fault is 1.7-2.4 Ma
562 based on the Quaternary vertical displacement rate of 0.8-1.2 mm yr⁻¹ and the vertical height
563 (2000 m) of the fault-bounded Jargalant Mountain, which is topped by a peneplain surface.
564 They assume that the initiation of faulting coincides with the onset of mountain building, as
565 the mountains are formed along restraining bends in the fault. Given the total offset-
566 constraints on the age of the fault, we favour the 'young fault' explanation for the lack of
567 observable rotation in the Zereg Basin, and therefore suggest this is indicative of the
568 expansion of the region of active faulting eastwards from the central Altay through time.
569 Using an initiation age of 1.7-2.4 Ma, we can infer a rate of anticlockwise rotation not
570 exceeding 2.9 – 4 degrees/Ma, with no lower bound.

571 The strike of the Har-Us-Nuur fault compared to other faults within the Altay is also indicative
572 of a shorter duration of activity and widening of the mountain range. The transpressional
573 Altay faults are characterised by anastomosing segments that on average strike NNW – SSE
574 (Figure 3). In general, fault segments that strike more northerly are dominated by strike-slip
575 motion. Segments that strike towards the west have a greater reverse component of slip, or
576 have at least developed branching reverse faults and flower structures (Figure 3;
577 Cunningham, 2005). Faults in the interior parts of the range trend more towards the west
578 (~314 – 330°), due to having a longer history of activity during which they accumulated more
579 anticlockwise rotation than the Har-Us-Nuur fault, which has a strike of 330 – 347°.

580 *5.3 Implications for the timing and evolution of deformation in the Altay and central Asia*

581 Thermochronologic studies from across the Altay are not in agreement on the initiation age
582 of deformation in the region, and this has implications for the northwards propagation of the
583 India-Asia collision. Many authors (e.g. Buslov et al., 2008; De Grave et al., 2007; Yin, 2010)
584 reference young thermochronologic ages from the Altay and nearby Gobi Altay to imply that
585 deformation has propagated over time and space northwards, through the Tien Shan and only
586 recently into the Altay and Siberian plate margin. Apatite fission track (AFT) results from the
587 Zereg Basin, some parts of the Siberian Altay, and the Gobi Altay place the initiation of
588 deformation around 5 Ma, assuming that modelled cooling ages represent the onset of uplift
589 of a widespread Jurassic planation surface preserved at the tops of mountains in these areas
590 (De Grave et al., 2007; Jolivet et al., 2007; Vassallo, 2006). However both AFT and U-Th/He
591 data from the Siberian part and central spine of the Altay hint at a longer-lived history of
592 deformation, initiating sometime in the Oligocene to early Miocene (De Grave et al., 2007;
593 Glorie et al., 2012a; Glorie et al., 2012b; Yuan et al., 2006). The central spine of the Altay also
594 lacks a widespread planation surface, also suggesting that uplift may be more long-lived in
595 this region, allowing more time for slow erosive processes to degrade the peneplain.

596 The lack of rotation measured in this study combined with the more recent
597 thermochronologic data (Glorie et al., 2012a; Glorie et al., 2012b) supports a long-lived
598 history of deformation in the Altay, with progressive widening of the range through time. This
599 was first hypothesised by Nissen et al. (2009b), who suggested that older faults in the interior
600 of the Altay rotate to less-favourable orientations and strain migrates outwards towards more
601 favourably oriented structures and areas of lower topography to minimise the work done
602 against gravity. Both the Har-Us-Nuur fault on the eastern margin of the range and the Fu Yun
603 fault on the western margin strike more northerly (330 – 347°) and are thus inferred to be
604 younger than faults in the high and compact central Altay mountains which on average strike
605 more towards the west (~314 – 330°). Our palaeomagnetic data from the exterior of the range
606 are in agreement with the hypotheses in Nissen et al. (2009b). It is likely that the major faults
607 in the Altay have initiated as nearly pure strike slip faults, with a more northerly strike that
608 followed the regional structural fabric and was not optimally-oriented with respect to the
609 regional SH_{max} of the India-Asia collision. New faults were prone to anticlockwise rotation to
610 accommodate the regional strain field, which placed them at a higher angle to SH_{max} as

611 rotation progressed. This encouraged the development of the flower structures present
612 across the central Altay which have branching reverse faults (e.g. Figure 3), because steeply
613 dipping strike-slip faults do not accommodate significant uplift. The evolving process of
614 deformation in the Altay has led to continuous mountain topography in the oldest parts of
615 the mountain range as structures coalesced. Strain partitioning in the Altay has not advanced
616 to the point such that the original generation of strike-slip faults have become inactive,
617 because there is clear evidence for neotectonic activity on strike-slip faults in the central part
618 of the mountain range (Frankel et al., 2010; Gregory et al., 2014), many of which do strike
619 more towards the north due to the anastomosing pattern of fault traces (Figure 3).

620 Other authors have used the lack of rotation measured on faults in central Asia to discuss
621 fault strength. van Hinsbergen et al. (2008) used the lack of rotation measured very close to
622 the Bogd fault in the Gobi Altay to suggest that the fault is weak, allowing strain to be localised
623 onto the fault, as otherwise they would have observed at least some local rotation. They also
624 suggest that strike-slip faulting in the range is subordinate to thrust faulting, despite the M
625 8.3 left-lateral strike slip earthquake that occurred in 1957 (see Figure 1 for the location of
626 the Bogd fault). However, in the case of the Bogd fault, rotation is simply not required by the
627 kinematics of faulting in the Gobi Altay, where fault strikes are aligned with the regional GPS
628 velocities (Figure 2), and so the lack of rotation cannot be used to infer fault strength.
629 Similarly, the lack of rotation we measure in this study cannot be used to comment on fault
630 strength because the lack of rotation on the Har-Us-Nuur fault is due to its young age of
631 initiation, and it has not been active for a sufficiently long time (e.g. > 5 m.y.) to have
632 accumulated measurable palaeomagnetic rotation.

633 **6. Conclusions**

634 We present the second palaeomagnetic study from Cenozoic rocks conducted in the Altay.
635 Samples collected from the Zereg Basin in the eastern Altay provide reliable palaeomagnetic
636 directions that pass a fold test and include a magnetic reversal. The declinations are not
637 significantly rotated with respect to the expected directions, which is in contrast with anti-
638 clockwise rotations of $39 \pm 8^\circ$ estimated from the Chuya Basin in the Siberian Altay. The lack
639 of palaeomagnetic rotations on the Har-Us-Nuur fault suggest that this fault is significantly
640 younger than the faults surrounding the Chuya Basin in the central Altay, and cannot have

641 rotated more than 7° in the past 5 m.y. Our work is in agreement with the young age of
642 initiation inferred by Nissen et al. (2009b; 1.7 - 2.4 Ma), and fits with the model of deformation
643 in the Altay where strike-slip faults progressively rotate as they accumulate displacement,
644 forming flower structures. Generally straight pure strike-slip faults striking closer to N-S are
645 younger than those with a more NW-SE orientation. This model is the result of strain being
646 accommodated on a pre-existing structural grain and rotating to accommodate regional
647 $S_{H_{max}}$. The style of mountain building in the Altay is in contrast with compressional
648 deformation regimes across central Asia where thrust faulting dominates some mountain
649 belts (e.g. the Tien Shan), and left-lateral non-rotational shear arises elsewhere (e.g. the Gobi
650 Altay). More work is needed to unravel the relationship between the complexity of the
651 surface trace of faults where they have rotated, and how vertical axis rotation in general
652 influences the evolving pattern of deformation in an active transpressional mountain range.

653 **Tables**

654 **Table 1:** Palaeomagnetic sampling site localities, ages, and bedding orientations

655 **Table 2:** Site-averaged palaeomagnetic data and VGP comparisons (attached).

656 **Figures**

657 **Figure 1:** (a) SRTM shaded relief image of the Altay and (b) the India-Asia collision zone,
658 produced using the Generic Mapping Tools software (GMT, Wessel et al., 2013). In (a)
659 earthquake focal mechanisms are from Sloan et al. (2011), Nissen et al. (2007), and
660 Bayasgalan et al. (2005, other references within), with $M_w > 7$ events indicated. Active faults
661 are plotted in black (Baljinnyam et al., 1993; Gregory, 2012). (b) SRTM topography and major
662 tectonic boundaries of the India-Eurasia collision.

663

664 **Figure 2:** (a) SRTM shaded relief image of the Altay. GPS velocities are relative to stable
665 Eurasia and suggest $\sim 7 \text{ mm yr}^{-1}$ of northeast-directed shortening across the Altay (Calais et
666 al., 2006; Yang et al., 2008). Active faults are plotted in grey (Baljinnyam et al., 1993; Gregory,
667 2012). (b) Schematic diagram for deformation in Mongolia, with rotation on dextral faults in
668 the Altay (W Mongolia), and non-rotational shear required across the Gobi Altay and central

669 Mongolia, following the pattern of GPS-derived velocity vectors plotted in (a). In this
670 kinematic model, w indicates the average spacing between faults and θ is the degree of
671 rotation for an amount d of fault displacement after Walker and Jackson (2004) and described
672 in section 5.2.

673 **Figure 3:** Map of the Altay Mountains and active strike-slip faults. Black strain crosses show
674 the principal strain axes (compressional arrows point in, extensional arrows point out) from
675 Kreemer et al. (2014). Quaternary slip rates are noted in blue from Frankel et al. (2010);
676 Gregory et al. (2014); Nissen et al. (2009a); Nissen et al. (2009b); and Vassallo (2006). Rotation
677 estimates are plotted as rotational wedges in radians from north (white) with uncertainties
678 (grey) for the Chuya Basin (Thomas et al., 2002) and Zereg Basin (this study, each wedge
679 division is 2 radians). Coloured dots (earthquake locations) and arrows (earthquake slip
680 vectors) are for first-motion mechanisms (yellow; Bayasgalan et al., 2005, and references
681 therein), waveform-modelled solutions (red; Sloan et al., 2011, and references therein), and
682 from the Global CMT Catalogue (orange). Earthquake slip vectors are only plotted where the
683 fault plane is reliably established by field or remote mapping of the active trace. Where
684 discrimination between the fault and auxiliary plane is not possible, no slip vector is plotted.

685 **Figure 4:** (a) Landsat image (RGB = 741) of the Zereg Basin, with the three different sampling
686 localities indicated (North, North east, and South west). Figure 4 is indicated by dashed box.
687 Abbreviations are BHU: Baatar Hyarhan Uul, BU: Bumbat Uul, HF: Hovd Fault, HUN: Har-Us-
688 Nuur, HUNF: Har-Us-Nuur Fault, and JU: Jargalant Uul. The town of Zereg is indicated. (b) and
689 (c) are ASTER images of the northern and south-western sampling localities, with sample sites
690 labelled.

691 **Figure 5:** ASTER imagery (15 m/pixel) of the sampling sites from the northeast side of the
692 Zereg Basin. The lower panel shows a geological map of the area modified from Howard et al.
693 (2003) and (Nissen et al., 2009a), with the ages of the units mapped labelled and sampling
694 localities indicated. The region includes a syncline-anticline pair.

695 **Figure 6:** Photos of the exposures of Cenozoic and Mesozoic sediments in the northeast and
696 southeast Zereg Basin. (a) Outcrop of the upper red-bed unit, with strata uplifted by
697 southwest-dipping thrust faults (site 8). (b) Upper Red Bed Plio-Pleistocene sediments
698 uplifted on the flanks of Baatar Hyarhan Mountain, dipping SW towards the peaks of Baatar

699 Hyarhan in the background (sites 14-16). (c) Cretaceous sandstones with palaeomagnetic drill
700 holes at site 6. (d) Oligocene Oasis Unit, with interbedded red sandstones (sampled, site 12)
701 and yellow sandstones with cross bedding.

702 **Figure 7:** Example thermal demagnetisation Zijderveld diagrams from each rock unit sampled.
703 Plots are shown tilt-corrected with a tectonic correction for the orientation of the strata
704 sampled. Open points indicate the inclination, and closed points are the sample declination.
705 North is to the right of the plot, and magnetic declinations are fit as vectors through
706 measurements from high to low temperature.

707 **Figure 8:** Results from Curie temperature tests on four example samples. TcH indicates the
708 Curie temperature when heating, which is indicated by a sharp drop in susceptibility. TcC is
709 the Curie temperature during cooling, and is the end of the steep increase in susceptibility
710 during cooling. Most samples show some alteration during heating, evidenced by the higher
711 susceptibility during cooling than heating, although this is not observed in site 1. Samples
712 have Curie temperatures around 560 – 580°C, indicating that magnetite is the primary
713 magnetic carrier. Site 3 shows a steepening in slope at around 650°C, which may indicate the
714 presence of hematite.

715 **Figure 9:** *In-situ* and tilt corrected site means and α_{95} cones of uncertainty are shown on the
716 stereoplots (lower hemisphere projection) for all stable and consistent sites (site numbers
717 are labelled). Closed circles indicate positive directions and open circles indicate negative
718 directions, and all sites are plotted as a single (normal) polarity. The lower panel shows the
719 results of the fold test that includes all sites, with a higher K value, indicating greater
720 precision, with 90-100% unfolding.

721 **Figure 10:** Age mean palaeomagnetic directions compared to the reference VGP poles we
722 calculated for Mongolia (Torsvik et al., 2012). Our directions reflect some inclination
723 shallowing but no rotation of the declination, within the error of the measurements.

724 **Acknowledgements:**

725 LCG thanks the Oxford Clarendon Fund and Burdet-Coutts fund for support during her PhD.
726 During this work, RTW was supported by the Royal Society of London through a University
727 Research Fellowship, and TJC through a Research Fellowship from the Royal Commission for

728 the Exhibition of 1851. NERC is thanked for its support through NCEO/COMET and for
729 supporting LCG through an Independent Research Fellowship. We thank Alex Densmore and
730 Tony Watts for comments on an early draft of this manuscript, and three anonymous
731 reviewers for constructive comments that improved the manuscript. We thank Nara, Deegi,
732 and Amgaa for their valuable assistance in the field, and Bayasgalan Amgalan for his role in
733 organising our fieldwork.

734

735 **References**

736

- 737 Abdrakhmatov, K.Y., Aldazhanov, S.A., Hager, B.H., Hamburger, M.W., Herring, T.A., Kalabaev, B.,
738 Makarov, V.I., Molnar, P., Panasyuk, S.V., Prilepin, M.T., Reilinger, R.E., Sadybakasov, I.S., Souter, B.J.,
739 Trapeznikov, Y.A., Tsurkov, V.Y., Zubovich, A.V., 1996. Relative recent construction of the Tien Shan
740 inferred from GPS measurements of present-day crustal deformation rates. *Nature* 384, 450-453.
- 741 Badarch, G., Byamba, J., Mahbadar, T., Minjin, C., Orolmaa, D., Tomurtogoo, O., Khosbayar, T., 1998.
742 Geological Map of Mongolia, in: Mineral Resources Authority of Mongolia, G.S. (Ed.). Mongolian
743 Academy of Sciences, Institute of Geology and Mineral Resources, Ulaanbataar.
- 744 Badarch, G., Cunningham, W.D., Windley, B.F., 2002. A new terrane subdivision for Mongolia:
745 implications for the Phanerozoic crustal growth of Central Asia. *Journal of Asian Earth Sciences* 21, 87-
746 110.
- 747 Baljinnyam, I., Bayasgalan, A., Borisov, B.A., Cisternas, A., Dem'yanovich, M.G., Ganbaatar, L.,
748 Kochetkov, V.M., Kurushin, R.A., Molnar, P., Philip, H.e., Vashchilov, Y.Y., 1993. Ruptures of major
749 earthquakes and active deformation in Mongolia and its surroundings, *Geological Society of America*
750 *Memoir*. The Geological Society of America, pp. 1-61.
- 751 Bayasgalan, A., Jackson, J., McKenzie, D., 2005. Lithosphere rheology and active tectonics in Mongolia:
752 relations between earthquake source parameters, gravity, and GPS measurements. *Geophysical*
753 *Journal International* 163, 1151-1179.
- 754 Briggs, S.M., Yin, A., Manning, C.E., Chen, Z.-L., Wang, X.-F., 2009. Tectonic development of the
755 southern Chinese Altai Range as determined by structural geology, thermobarometry, $^{40}\text{Ar}/^{39}\text{Ar}$
756 thermochronology, and Th/Pb ion-microprobe monazite geochronology. *Geological Society of*
757 *America Bulletin* 121, 1381-1393.
- 758 Buslov, M.M., Kokh, D.A., De Grave, J., 2008. Mesozoic-Cenozoic tectonics and geodynamics of Altai,
759 Tien Shan, and Northern Kazakhstan, from apatite fission-track data. *Russian Geology and Geophysics*
760 49, 648-654.
- 761 Calais, E., Dong, L., Wang, M., Shen, Z., Vergnolle, M., 2006. Continental deformation in Asia from a
762 combined GPS solution. *Geophysical Research Letters* 33, L24319.
- 763 Calais, E., Vergnolle, M., San'kov, V., Likhnev, A., Miroshnitchenko, A., Amarjargal, S., Deverchere, J.,
764 2003. GPS measurements of crustal deformation in the Baikal-Mongolia area (1994-2002):
765 Implications for current kinematics of Asia. *Journal of Geophysical Research* 108, 2501-2513.
- 766 Campbell, G.E., Walker, R.T., Abdrakhmatov, K.Y., Schwenninger, J.L., Jackson, J.A., Elliott, J.R., Copley,
767 A., 2013. The Dzhungarian fault: Late Quaternary tectonics and slip rate of a major right-lateral strike-
768 slip fault in the northern Tien Shan region. *Journal of Geophysical Research: Solid Earth* 118, 5681-
769 5698.
- 770 Cowgill, E., Arrowsmith, J.R., Yin, A., Xiaofeng, W., Zhengle, C., 2004. The Akato Tagh bend along the
771 Altyn Tagh fault, northwest Tibet 2: Active deformation and the importance of transpression and strain
772 hardening within the Altyn Tagh system. *GSA Bulletin* 116, 1443-1464.

773 Cunningham, D., Davis, S., Badarch, G., 2003a. Crustal architecture and active growth of the Suta
774 Range, western Mongolia: a major intracontinental, intraplate restraining bend. *Journal of*
775 *Geodynamics* 36, 169-191.

776 Cunningham, D., Dijkstra, A., Howard, J., Quarles, A., Badarch, G., 2003b. Active intraplate strike-slip
777 faulting and transpressional uplift in the Mongolian Altai, Special Publications. Geological Society,
778 London, pp. 65-87.

779 Cunningham, W.D., 1998. Lithospheric controls on late Cenozoic construction of the Mongolian Altai.
780 *Tectonics* 17, 891-902.

781 Cunningham, W.D., 2005. Active intracontinental transpressional mountain building in the Mongolian
782 Altai: Defining a new class of orogen. *Earth and Planetary Science Letters* 240, 436-444.

783 Cunningham, W.D., 2007. Structural and topographic characteristics of restraining bend mountain
784 ranges of the Altai, Gobi Altai and easternmost Tien Shan, Geological Society, London, Special
785 Publications. The Geological Society of London, pp. 219-237.

786 Cunningham, W.D., 2011. Cenozoic normal faulting and regional doming in the southern Hangay
787 region, Central Mongolia: implications for the origin of the Baikal rift province. *Tectonophysics* 331,
788 389-411.

789 Cunningham, W.D., Windley, B.F., Dorjnamjaa, D., Badamgarov, G., Saandar, M., 1996. A structural
790 transect across the Mongolian Western Altai: Active transpressional mountain building in central Asia.
791 *Tectonics* 15, 142-156.

792 De Grave, J., Buslove, M.M., Van den haute, P., 2007. Distant effects of India-Eurasia convergence and
793 Mesozoic intracontinental deformation in Central Asia: Constraints from apatite fission-track
794 thermochronology. *Journal of Asian Earth Sciences* 29, 188-204.

795 De Grave, J., Van den haute, P., 2002. Denudation and cooling of the Lake Teletskoye Region in the
796 Altai Mountains (South Siberia) as revealed by apatite fission-track thermochronology. *Tectonophysics*
797 349, 145-159.

798 De Grave, J., Van den haute, P., Buslove, M.M., Dehandschutter, B., Glorie, S., 2008. Apatite fission-
799 track thermochronology applied to the Chulyshman Plateau, Siberian Altai, Region. *Radiation*
800 *Measurements* 43, 38-42.

801 Demarest, H.H., 1983. Error analysis for the determination of tectonic rotation from paleomagnetic
802 data. *Journal of Geophysical Research* 88, 4321-4328.

803 Devyatkin, E.V., 1981. The Cenozoic of Inner Asia stratigraphy, geochronology and correlation, in:
804 Nikiforova, K.V. (Ed.), *Comb. Sov-Mongolian Sci. Res. Geol. Exped. Transactions*, Nauka, Moscow. (In
805 Russian).

806 Devyatkin, E.V., Martinson, G.G., Shuwalov, V.F., Khosbayar, P., 1975. Stratigraphy of Mesozoic
807 deposits of Mongolia. The Joint Soviet-Mongolian Scientific Research Geological Expedition,
808 Leningrad, Nauka (in Russian) 13, 25-49.

809 Dupont-Nivet, G., Guo, Z., Butler, R.F., Jia, C., 2002. Discordant paleomagnetic direction in Miocene
810 rocks from the central Tarim Basin: evidence for local deformation and inclination shallowing. *Earth*
811 *and Planetary Science Letters* 199, 472-482.

812 England, P., Molnar, P., 1990. Right-lateral shear and rotation as the explanation for strike-slip faulting
813 in eastern Tibet. *Nature* 344, 140-143.

814 Fisher, R.A., 1953. Dispersion on a sphere. *Proceedings of the Royal Society of London, Series A* 217,
815 295-305.

816 Frankel, K.L., Wegmann, K.W., Bayasgalan, A., Carson, R.J., Bader, N.E., Adiya, T., Bolor, E., Durfey, C.C.,
817 Otgonkhuu, J., Sprajcar, J., Sweeney, K.E., Walker, R.T., Marsteller, T.L., Gregory, L.C., 2010. Late
818 Pleistocene slip rate of the Höh Serh-Tsagaan Salaa fault system, Mongolian Altai and intracontinental
819 deformation in central Altai. *Geophysical Journal International* 183, 1134-1150.

820 Gan, W., Zhang, P., Shen, Z.-K., Niu, Z., Wang, M., Wan, Y., Zhou, D., Cheng, J., 2007. Present-day crustal
821 motion within the Tibetan Plateau inferred from GPS measurements. *Journal of Geophysical Research*
822 112, B08416.

823 Glorie, S., De Grave, J., Buslov, M.M., Zhimulev, F.I., Elburg, M.A., Van den haute, P., 2012a. Structural
824 control on Meso-Cenozoic tectonic reactivation and denudation in the Siberian Altai: insights from
825 multi-method thermochronometry. *Tectonophysics* 544-545, 75-92.

826 Glorie, S., De Grave, J., Delvaux, D., Buslov, M.M., Zhimulev, F.I., Vanhaecke, F., Elburg, M.A., 2012b.
827 Tectonic history of the Irtysh shear zone (NE Kazakhstan): new constraints from zircon U/Pb dating,
828 apatite fission track dating and palaeostress analysis. *Journal of Asian Earth Sciences* 45, 138-149.

829 Gregory, L.C., 2012. Active Faulting and Deformation of the Mongolian Altay Mountains, Department
830 of Earth Sciences. University of Oxford.

831 Gregory, L.C., Thomas, A.L., Walker, R.T., Garland, R., Mac Niocaill, C., Fenton, C.R., Bayasgalan, A.,
832 Amgaa, T., Gantulga, B., Xu, S., Schnabel, C., West, A.J., 2014. Combined uranium series and ¹⁰Be
833 cosmogenic exposure dating of surface abandonment: a case study from the Ölgii strike-slip fault in
834 western Mongolia. *Quaternary Geochronology* 24, 27-43.

835 Howard, J.P., Cunningham, W.D., Davies, S.J., Dijkstra, A.H., Badarch, G., 2003. The stratigraphic and
836 structural evolution of the Dzereg Basin, western Mongolia: clastic sedimentation, transpressional
837 faulting and basing destruction in an intraplate, intercontinental setting. *Basin Research* 15, 45-72.

838 Jolivet, M., Ritz, J.F., Vassallo, R., Larroque, C., Braucher, R., Todbileg, M., Chauvet, A., Sue, C., Arnaud,
839 N., De Vicente, R., Arzhanikova, A., Arzhanikov, S., 2007. Mongolian summits: An uplifted, flat, old but
840 still preserved erosion surface. *Geology* 35, 871-874.

841 Khosbayar, P., 1973. New data on Upper Jurassic and Lower Cretaceous sediments of western
842 Mongolia. *Academy of Sciences, USSR, Doklady (Earth Sciences Section)* 208, 115-116.

843 Klinger, Y., Etchebes, M., Tapponnier, P., Narteau, C., 2011. Characteristic slip for five great
844 earthquakes along the Fuyun fault in China. *Nature Geoscience* 4, 389-392.

845 Kreemer, C., Blewitt, G., Klein, E.C., 2014. A geodetic plate motion and Global Strain Rate Model.
846 *Geochemistry, Geophysics, Geosystems* 15, 3849-3889.

847 Lukhnev, A.V., San'kov, V.A., Miroshnitchenko, A.I., Ashurkov, S.V., Calais, E., 2010. GPS rotation and
848 strain rates in the Baikal-Mongolia region. *Russian Geology and Geophysics* 51, 785-793.

849 McElhinny, M.W., 1964. Statistical significance of the fold test in palaeomagnetism. *Geophysical*
850 *Journal of the Royal Astronomical Society* 8, 338-340.

851 Meade, B.J., 2007. Present-day kinematics at the India-Asia collision zone. *Geology* 35, 81-84.

852 Merrill, R.T., McElhinny, M.W., McFadden, P.L., 1998. *The Magnetic Field of the Earth*. Academic Press.

853 Molnar, P., Ghose, S., 2000. Seismic moments of major earthquakes and the rate of shortening across
854 the Tien Shan. *Geophysical Research Letters* 27, 2377-2380.

855 Nissen, E., Emmerson, B., Funning, G., Mistrukov, A., Parsons, B., Robinson, D.P., Rogozhin, E., Wright,
856 T.J., 2007. Combining InSAR and seismology to study the 2003 Siberian Altai earthquakes--dextral
857 strike-slip and anticlockwise rotations in the northern India-Eurasia collision zone. *Geophysical Journal*
858 *International* 169, 216-232.

859 Nissen, E., Walker, R., Molor, E., Fattahi, M., 2009a. Late Quaternary rates of uplift and shortening at
860 Baatar Hyarhan (Mongolian Altai) with optically stimulated luminescence. *Geophysical Journal*
861 *International* 177, 259-278.

862 Nissen, E., Walker, R.T., Bayasgalan, A., Carter, A., Fattahi, M., Molor, E., Schnabel, C., West, A.J., Xu,
863 S., 2009b. The late Quaternary slip-rate of the Har-Us-Nuur fault (Mongolian Altai) from cosmogenic
864 ¹⁰Be dates and luminescence dating. *Earth and Planetary Science Letters* 286, 467-478.

865 Scholz, C.H., Ando, R., Shaw, B.E., 2010. The mechanics of first order splay faulting: The strike-slip case.
866 *Journal of Structural Geology* 32, 118-126.

867 Sengör, A.M.C., Natal'in, B.A., Burtman, V.S., 1993. Evolution of the Altaid tectonic collage and
868 Palaeozoic crustal growth in Eurasia. *Nature* 364, 299-307.

869 Shuvalov, V.F., 1968. More information about Upper Jurassic and Lower Cretaceous in the southeast
870 Mongolian Altai. *Academy of Sciences, USSR, Doklady (Earth Sciences Section)* 197, 31-33.

871 Shuvalov, V.F., 1969. Continental redbeds of the Upper Jurassic of Mongolia. *Academy of Sciences,*
872 *USSR, Doklady (Earth Sciences Section)* 189, 112-114.

873 Sjostrom, D.J., Hendrix, M.S., Badamgarav, D., Graham, S.A., Nelson, B.K., 2001. Sedimentology and
874 provenance of Mesozoic nonmarine strata in western Mongolia: a record of intracontinental
875 deformation, Palaeozoic and Mesozoic tectonic evolution of Central and Eastern Asia: from
876 continental assembly to intracontinental deformation. *Geological Society of America Memoir*, pp. 361-
877 388.

878 Sloan, R.A., Jackson, J.A., McKenzie, D., Priestley, K., 2011. Earthquake depth distributions in central
879 Asia, and their relations with lithosphere thickness, shortening and extension. *Geophysical Journal
880 International* 185, 1-29.

881 Tauxe, L., 2010. *Essentials of Paleomagnetism*. University of California Press.

882 Tauxe, L., Kent, D.V., 2004. A simplified statistical model for the geomagnetic field and the detection
883 of shallow bias in paleomagnetic inclinations: was the ancient magnetic field dipolar?, *Timescales of
884 the Paleomagnetic field*. American Geophysical Union, Washington, DC, pp. 101-115.

885 Thomas, J.C., Lanza, R., Kazansky, A., Zykin, V., Semakov, N., Mitrokhin, D., Delvaux, D., 2002.
886 Paleomagnetic study of Cenozoic sediments from the Zaisan basin (SE Kazakhstan) and the Chuya
887 depression (Siberian Altai): tectonic implications for central Asia. *Tectonophysics* 351, 119-137.

888 Thomas, J.C., Perroud, H., Cobbold, P., Bazhenov, M., Burtman, V.S., Chauvin, A., Sdybakasov, E., 1993.
889 A paleomagnetic study of Tertiary formations from the Kyrgyz Tien-Shan and its tectonic implications.
890 *J Geophys Res* 98, 9571-9589.

891 Torsvik, T.H., Van der Voo, R., Preeden, U., Mac Niocaill, C., Steinberger, B., Doubrovine, P.V., van
892 Hinsbergen, D.J.J., Domeir, M., Gaina, C., Tohver, E., Meert, J.G., McCausland, P.J.A., Cocks, L.R.M.,
893 2012. Phanerozoic Polar Wander, Palaeogeography and Dynamics. *Earth Science Reviews* 114, 325-
894 368.

895 Van der Voo, R., 1989. Paleomagnetism of North America: The craton, its margins, and the
896 Appalachian Belt, in: Pakiser, L.C., Mooney, W.D. (Eds.), *Geophysical Framework of the Continental
897 United States*, Geol. SOC. Am. Mem. Geological Society of America, Washington, DC, pp. 447-470.

898 van Hinsbergen, D.J.J., Straathof, G.B., Kuiper, K.F., Cunningham, W.D., Wijbrans, J., 2008. No vertical
899 axis rotations during Neogene transpressional orogeny in the NE Gobi Altai: coinciding Mongolian and
900 Eurasian early Cretaceous apparent polar wander paths. *Geophysical Journal International* 173, 105-
901 126.

902 Vassallo, R., 2006. *Chronologie et evolution des reliefs dans la region Mongolie-Siberie: approach
903 morphotectonique et geochronologique*. L'Universite Montpellier II.

904 Vassallo, R., Jolivet, M., Ritz, J.F., Braucher, R., Larroque, C., Sue, C., Todbileg, M., Javkhlanbold, D.,
905 2007. Uplift age and rates of the Gurvan Bogd system (Gobi Altay) by apatite fission track analysis.
906 *Earth and Planetary Science Letters* 259, 333-346.

907 Walker, R., Jackson, J., 2004. Active tectonics and late Cenozoic strain distribution in central and
908 eastern Iran. *Tectonics* 23.

909 Walker, R.T., Bayasgalan, A., Carson, R., Hazlett, R., McCarthy, L., Mishler, J., Molor, E., Sarantsetseg,
910 P., Smith, L., Tsogtbadrakh, B., Tsolmon, G., 2006. Geomorphology and structure of the Jid right-lateral
911 strike-slip fault in the Mongolian Altay mountains. *Journal of Structural Geology* 28, 1607-1622.

912 Walker, R.T., Jackson, J.A., 2002. Offset and evolution of the Gowk fault, S.E. Iran: a major intra-
913 continental strike-slip system. *Journal of Structural Geology* 24, 1677-1698.

914 Walker, R.T., Nissen, E., Molor, E., Bayasgalan, A., 2007. Reinterpretation of the active faulting in
915 central Mongolia. *Geology* 35, 759-762.

916 Wang, Q., Zhang, P.-Z., Freymuller, J.T., Bilham, R., Larson, K.M., Lai, X.a., You, X., Niu, Z., Wu, J., Li, Y.,
917 Liu, J., Yang, Z., Chen, Q., 2001. Present-day crustal deformation in China constrained by Global
918 Positioning System measurements. *Science* 294, 574-576.

919 Weil, A.B., Sussman, A.J., 2004. Classifying curved orogens based on timing relationships between
920 structural development and vertical-axis rotations, in: Sussman, A.J., Weil, A.B. (Eds.), *Orogenic
921 Curvature: Integrating Paleomagnetic and Structural Analyses: Geological Society of America Special
922 Paper*, pp. 1-15.

923 Wessel, P., Smith, W., Scharroo, R., Luis, J., Wobbe, F., 2013. Generic Mapping Tools: Improved version
924 released. EOS Transactions AGU 94, 409-410.
925 Yang, S., Li, J., Wang, Q., 2008. The deformation pattern and fault rate in the Tianshan Mountains
926 inferred from GPS observations. Science in China Series D: Earth Sciences 51, 1064-1080.
927 Yin, A., 2010. Cenozoic tectonic evolution of Asia: A preliminary synthesis. Tectonophysics 488, 293-
928 325.
929 Yuan, W., Carter, A., Dong, J., Bao, Z., An, Y., Guo, Z., 2006. Mesozoic-Tertiary exhumation history of
930 the Altai Mountains, northern Xinjiang, China: new constraints from apatite fission track data.
931 Tectonophysics 412, 183-193.
932 Zhang, P.-Z., Shen, Z., Wang, M., Gan, W., Burgmann, R., Molnar, P., Wang, Q., Niu, Z., Sun, J., Wu, J.,
933 Hanrong, S., Xinzhao, Y., 2004. Continuous deformation of the Tibetan Plateau from global positioning
934 system data. Geology 32, 809-812.
935 Zijdeveld, J.D.A., 1967. AC demagnetization of rocks: analysis of results, Methods in
936 Palaeomagnetism. Elsevier, Amsterdam, pp. 245-286.
937 Zuza, A.V., Yin, A., 2016. Continental deformation accommodated by non-rigid passive bookshelf
938 faulting: An example from the Cenozoic tectonic development of northern Tibet. Tectonophysics 677-
939 678, 227-240.

940